TXNDC5 Governs Extracellular Matrix Homeostasis in Pulmonary Hypertension

Zhen Chen[1*]; Fanhao Kong[1*]; Lixin Huang[1*]; Wenze Wu[1*]; Ziping Wang[1]; Hanbin Chen[1]; Junting Zhang[1]; Lin Deng[6]; Chengrui Cao[1]; Xiaoyan Zhang[1]; Zixin Liu[2]; Kai-Chien Yang[3#]; Wei-Ting Chang[4, 5#]; Jin-Song Bian[1#]; Xiaowei Nie[2#];

1 Department of Pharmacology, Joint Laboratory of Guangdong-Hong Kong Universities for Vascular Homeostasis and Diseases, SUSTech Homeostatic Medicine Institute, School of Medicine, Southern University of Science and Technology, Shenzhen 518055, China.

2 Department of Human Cell Biology and Genetics, SUSTech Homeostatic Medicine Institute, School of Medicine, Southern University of Science and Technology, Shenzhen 518055, China.

3 Department and Graduate Institute of Pharmacology, National Taiwan University College of Medicine, Taipei, Taiwan

4 School of Medicine, College of Medicine, National Sun Yat-sen University, Kaohsiung, Taiwan

5 Division of Cardiology, Department of Internal Medicine, Chi Mei Medical Center, Tainan

6 Department of Cardiology, The Eighth Affiliated Hospital, Sun Yat-sen University, Shenzhen, China

[*]These authors contributed equally to this work.

[#]Correspondence to:

Xiaowei Nie, PhD, E-mail niexw@sustech.edu.cn.

Jin-Song Bian, PhD, E-mail bianjs@sustech.edu.cn.

Wei-Ting Chang, PhD, E-mail cmcvecho2@gmail.com.

Kai-Chien Yang, PhD, E-mail allenmy0920@gmail.com.

ABSTRACT

BACKGROUND: Pulmonary hypertension (PH) is characterized by vascular remodeling without effective treatments. Thioredoxin domain containing 5 (TXNDC5), a member of the protein disulfide isomerases (PDI) family, regulates protein folding and vascular homeostasis, yet its role in PH remains unknown.

METHODS: Label-free proteomics was used to profile PDI expression in hypoxic PH patients. TXNDC5 expression and localization were examined by multiplex immunofluorescence and Western blot. Gain- and loss-of-function approaches, including adeno-associated virus-mediated lung endothelial overexpression, global knockout, and endothelial ablation of TXNDC5, were used in Sugen5416/hypoxia (SuHx)-induced rodent PH models. *In vitro* endothelial cell assays, RNA sequencing, protein-protein interaction analysis, and pharmacological intervention were conducted to elucidate underlying mechanisms and therapeutic potential.

RESULTS: TXNDC5 was significantly upregulated in the lungs of both PH patients and experimental PH models, predominantly in endothelial cells of remodeled distal pulmonary arteries. Endothelial TXNDC5 overexpression exacerbated pulmonary vascular remodeling, elevated right ventricular systolic pressure, and promoted right ventricular hypertrophy, whereas global or endothelial-specific TXNDC5 deficiency conferred protection against SuHx-induced PH. RNA sequencing and protein-protein interaction analysis revealed that TXNDC5 regulated extracellular matrix homeostasis through biglycan (BGN), which was required for TXNDC5-mediated inhibition of HIF-1α/2α ubiquitination, leading to pathological HIF accumulation. Pharmacological inhibition of TXNDC5 with E64FC26 and endothelial-targeted TXNDC5 gene therapy significantly attenuated PH severity in SuHx rats.

CONCLUSIONS: Our study reveals that TXNDC5 is a main modulator to regulate ECM homeostasis and may serve as a promising target for the treatment of PH.

Key Words: pulmonary hypertension**,** extracellular matrix, TXNDC5, BGN, HIF signaling

INTRODUCTION

Pulmonary hypertension (PH) is a serious cardiovascular disease characterized by elevated pulmonary artery pressure and right heart failure, with high morbidity and mortality[1]. Hypoxia triggers PH, with Group III being common clinically[2]. Dysfunction of pulmonary artery endothelial cells (PAECs) under hypoxia initiates vasoconstriction[3], while pulmonary artery smooth muscle cells (PASMCs) become hyperproliferative and apoptosis-resistant phenotype, leading to vascular remodeling[4]. However, there remains no curative clinical treatment option for reversing remodeled vessels against the disease[5,6]. It highlights the need for further exploration of PH pathogenesis and new therapeutic targets.

Protein disulfide isomerase (PDI) is an endoplasmic reticulum enzyme family that mediates disulfide bond formation, protein folding, and regulates endothelial function to maintain vascular homeostasis[7,8]. PDIA1 controls HIF-1α expression and redox state via lysosomal degradation and enhances vascular endothelial growth factor receptor 2 signaling, promoting endothelial migration, proliferation, and angiogenesis[9,10]. TXNDC5, mainly expressed in endothelial cells (ECs) and also called endothelial PDI, is linked to fibrosis[11], diabetes[12], rheumatoid arthritis[13], and cancers[14]. Inhibition of TXNDC5 restores endothelial dysfunction to mitigate vascular calcification and atherosclerosis[15,16]. However, its role in pulmonary vascular remodeling in PH remains unclear.

Extracellular matrix (ECM) is a complex network of proteins and polysaccharides secreted by cells, providing structural and communicative support to adjacent cells[17]. Remodeling of pulmonary arterial ECM occurs in the early stage of PH pathogenesis, before increased wall thickness and pulmonary artery pressure. ECM remodeling is the cause rather than a consequence of pulmonary vascular remodeling in PH[18]. Recently, we revealed that the ECM proteins in PAECs accelerated pulmonary vascular remodeling through interaction with HIF-1α in a positive feedback loop manner, providing evidence for early intervention in ECM remodeling to prevent PH

progression[19,20].

In this study, using 4D label-free proteomics, we identified TXNDC5 as a markedly upregulated PDI protein in lungs of patients with hypoxic PH. Global or endothelial-specific deficiency of TXNDC5 alleviated Sugen5416/hypoxia (SuHx)-induced PH, whereas TXNDC5 overexpression aggravated PH. TXNDC5 silencing preserved ECM homeostasis, reduced PA remodeling, and restored endothelial function. In addition, TXNDC5 directly interacted with and assisted its the folding of biglycan (BGN), which was required to regulate the HIF-1α/2α ubiquitination. Pharmacological inhibition or pulmonary endothelium-targeted silencing of TXNDC5 effectively mitigated PH in rats. The present study therefore demonstrated for the first time that TXNDC5 may be a key protein to control ECM homeostasis and a promising therapeutic target for PH.

METHODS

Detailed expanded methods and materials are available in **Supplemental Material 1**.

Data Availability Statement

Source data and original blots or gel images for this study are available from the corresponding author upon reasonable request.

RESULTS

TXNDC5 Expression is Increased in PH Patients and Rodent Models

We performed 4D label-free proteomics on lung samples from 5 patients with hypoxic PH and 5 non-PH donors (**Figure S1A**). Among the human PDI family proteins, TXNDC5 was the most markedly dysregulated member in PH patients compared with donors (fold change=3.45, P=0.0048) (**Figure 1A**). Increased TXNDC5 expression in PH lungs was confirmed at both protein and mRNA levels (**Figure 1B-C**), and similarly observed in multiple rat and mouse PH models (**Figure 1D** and **Figure S1B**). In distal

117 pulmonary arteries (PAs), multiplex immunofluorescence (mIF) showed pronounced
118 co-localization of TXNDC5 with the endothelial marker CD31, α-SMA (a marker for
119 smooth muscle cells), and COL1A1 (a marker for fibroblasts) (**Figure 1E-G** and
120 **Figure S1C**). Furthermore, TXNDC5 was elevated in the intima of remodeled PAs
121 from interstitial lung disease (ILD)-PH and chronic obstructive pulmonary disease
122 (COPD)-PH patients (**Figure 1H**). Similar results were observed in the remodeled PAs
123 of SuHx- or monocrotaline (MCT)-induced PH rat models (**Figure 1I-K** and **Figure**
124 **S1D**). Western blot analysis of primary lung ECs corroborated these findings (**Figure**
125 **S1E-F**). Notably, intimal TXNDC5 levels positively correlated with right ventricular
126 systolic pressure (RVSP) and Fulton index (right ventricle weight to left ventricle plus
127 interventricular septum weight, ie, RV/(LV+S)), and negatively with tricuspid annular
128 plane systolic excursion (TAPSE) (**Figure 1L-N**). Taken together, these findings
129 suggest that the TXNDC5 may be a critical dysregulated factor in ECs within the
130 pulmonary vasculature that contributes to PH pathogenesis.
131
132 **TXNDC5 Mediates the Development of SuHx-Induced PH**
133 To investigate the role of TXNDC5 *in vivo* in the development of experimental
134 PH, TXNDC5 knockout (TXNDC5$^{-/-}$) mice were challenged with or without SuHx
135 (**Figure 2A**). TXNDC5 deletion alone had no significant effects but markedly reduced
136 RVSP (**Figure 2B**) and RV/(LV+S) (**Figure S2A**) induced by SuHx. Echocardiography
137 indicated improved right ventricular (RV) function, with increased PA acceleration
138 time/ PA ejection time ratio (PAT/PET), TAPSE, and right ventricular fractional area
139 change (RVFAC) (**Figure S2B-D**), and reduced right ventricular free wall thickness
140 (RVFWT) (**Figure S2E**). In addition, mIF and Victoria blue/Sirius red (VB/SR) showed
141 reduced distal PA muscularization, medial wall thickness, and collagen deposition
142 under SuHx (**Figure 2C-F**). Consistent with the PA changes, wheat germ agglutinin
143 (WGA) staining proved that the RV cardiomyocyte hypertrophy was markedly inhibited
144 in SuHx-treated TXNDC5$^{-/-}$ mice when compared with their control littermates (**Figure**
145 **2G**).
146 With a gain-of-function approach, an adeno-associated virus serotype engineered

to specifically target lung endothelial cells (AAV-TXN) was delivered via tail vein to overexpress TXNDC5 specifically in lung ECs (**Figure 2H**). *Ex vivo* imaging confirmed lung targeting (**Figure 2I**), and co-immunofluorescence and Western blot verified EC-specific overexpression (**Figure S2F-G**). Hemodynamic measurement revealed that mice administered with AAV-TXN increased the RVSP compared with those administered with control AAV (AAV-NC) even under normoxic conditions. In response to the SuHx challenge, AAV-TXN mice further increased in both RVSP and RV/(LV+S) (**Figure 2J** and **Figure S2H**). Echocardiography analysis showed reduced PAT/PET, TAPSE RVFAC, and increased RVFWT under SuHx (**Figure S2I-L**). In addition, mIF and VB/SR staining confirmed exacerbated distal PA remodeling with increased muscularization, medial thickness, and collagen deposition (**Figure 2K-N**). Conversely, endothelial TXNDC5 overexpression was found to exacerbate SuHx-induced PH.

Endothelial Cell-Specific Deletion of TXNDC5 Ameliorates SuHx-Induced PH

To examine the role of endothelial TXNDC5 in PH, endothelial cell-specific TXNDC5 knockout mice ($TXNDC5^{ECKO}$) were generated, validated (**Figure S2M**), and challenged by SuHx (**Figure 3A**). Deletion of endothelial TXNDC5 significantly attenuated SuHx-induced increases in RVSP (**Figure 3B**) and RV/(LV+S) (**Figure 3C**) and improved RV function **(Figure S2N-Q**). Under SuHx, $TXNDC5^{ECKO}$ mice exhibited reduced distal PA muscularization, medial wall thickness, and collagen deposition (**Figure 3D-G**). Lung angiography confirmed better intrapulmonary contrast filling in $TXNDC5^{ECKO}$ mice compared with $TXNDC5^{f/f}$ controls, indicating preserved pulmonary vasculature (**Figure 3H** and **Figure S2R**). In addition, SuHx-induced RV hypertrophy was also markedly attenuated, with decreased RV wall thickness and cardiomyocyte cross-sectional area (**Figure 3I-J**). Together, these findings underscore the crucial role of endothelial TXNDC5 in the development of PH and highlight its potential as a sex-independent therapeutic target.

TXNDC5 Promotes Hypoxia-Induced Dysfunction in Pulmonary Arterial Cells

Exposure to hypoxia significantly increased the TXNDC5 protein and mRNA levels in hPAECs, predominantly in the cytoplasm (**Figure S3A-C**). Silencing TXNDC5 with small-interfering RNA oligonucleotides (siTXNDC5) suppressed proliferation and migration of hPAECs under both normoxic and hypoxic conditions (**Figure S3D-E**), and prevented G1-to-S phase transition (**Figure S3F**). Conversely, TXNDC5 overexpression via lentivirus (LV-TXNDC5) disrupted cytoskeletal architecture, inducing prominent stress fibers and diffuse paxillin distribution (**Figure S3G-H**). Taken together, TXNDC5 regulates many important functional abnormalities associated with PH pathogenesis, with disruption of cytoskeletal architecture in hPAECs.

The hyper-proliferation and resistance to apoptosis of PASMCs directly accelerate the remodeling of PAs in PH[21]. Thus, we investigated whether endothelial TXNDC5 affects the function of hPASMCs via paracrine signaling. For this purpose, conditioned medium from siTXNDC5-treated hPAECs (siTXN-CM) was used to treat hPASMCs. Western blot showed that siTXN-CM significantly downregulated cyclin A and proliferating cell nuclear antigen (PCNA) expression under both normoxic and hypoxic conditions (**Figure S3I**). Consistently, EdU incorporation and Cell Counting Kit-8 (CCK-8) assays further confirmed that siTXN-CM suppressed the proliferation and viability of hPASMCs (**Figure S4A-B**). In addition, siTXN-CM enhanced hPASMCs apoptosis, as indicated by increased cleaved caspase-3 expression (**Figure S3J**). Collectively, our data demonstrate that hPAECs TXNDC5 plays a critical role in promoting hPASMCs proliferation, survival, and resistance to apoptosis.

TXNDC5 Regulates ECM Expression and Homeostasis

To explore the underlying downstream molecular mechanisms of TXNDC5, we performed a bulk RNA sequencing (RNA-seq) analysis on hPAECs transfected with siRNA targeting TXNDC5 under hypoxia exposure. Gene ontology analysis indicated that the silencing of TXNDC5 resulted in altered expression of genes mainly enriched in “collagen-containing ECM”, “ECM”, “ECM organization”, “ECM structural constituent”, “response to hypoxia”, and “cellular response to hypoxia” (**Figure 4A**).

We selected the differentially expressed ECM genes and then constructed a protein-protein interaction (PPI) network (**Figure 4B**). The network revealed that TXNDC5-affected ECM proteins were clustered into different functional subgroups, including "proteoglycans and glycoproteins", "collagens", "matrix modulators and adhesion", "metallopeptidase activity", "basement membrane", "growth factors and signaling regulators", and "angiogenesis". Immunofluorescence staining confirmed that periostin (POSTN), biglycan (BGN), lysyl oxidase (LOX), and transglutaminase 2 (TGM2) were excessively deposited in the PAs from $TXNDC5^{f/f}$ mice but not in $TXNDC5^{ECKO}$ mice under SuHx conditions (**Figure 4C-F** and **Figure S4C**). Western blot analysis also confirmed that TXNDC5 silencing reversed the abnormal expression of ECM proteins (COL1A1, TGM2, FN1, POSTN, LOX) induced by hypoxia treatment in hPAECs (**Figure 4G**).

To further investigate whether TXNDC5 regulates ECM secretion, we collected the supernatants from hPAECs. Dot blot analysis revealed that the silence of TXNDC5 markedly reduced the secretion of BGN, POSTN, and LOX **(Figure S4D-G)**. These results provide a mechanistic explanation for why the conditional medium from TXNDC5-silenced hPAECs suppresses proliferation and viability while promoting apoptosis of hPASMCs. Collectively, these data highlight the key role TXNDC5 played in regulating ECM homeostasis.

BGN Is a Promising Biomarker and Therapeutic Target for Hypoxic Pulmonary Hypertension

We next explored TXNDC5-targeted ECM proteins critical for EC function. We performed a computational analysis of the PPI network between the ECM proteins dataset and the ECs function-related proteins dataset. By integrating these datasets, we first constructed a comprehensive PPI network, which was then refined into a core network using degree-based filtering (**Figure 5A**). Through the intersection of ECM datasets, core ECM in the above PPI network, TXNDC5 silencing in hPAECs, and hypoxia-treated hPAECs (GSE160255), we finally identified biglycan (BGN) as a key candidate (**Figure S4H**).

BGN protein levels were increased in lung biopsies from patients with hypoxic PH or donors (**Figure S4I**). A GEO dataset (GSE254617) confirmed elevated BGN levels in idiopathic pulmonary arterial hypertension (IPAH) lungs (**Figure 5B**). Similarly, BGN was upregulated in rodent PH models (**Figure S4J-K**). We also investigated whether BGN can reflect the severity of PH by analyzing BGN levels in serum. Surprisingly, a markedly increased BGN level was found in the serum of 27 patients with hypoxic PH compared with the serum of 27 donors (**Figure 5C**). Serum BGN levels exhibited a significant correlation with systolic pulmonary artery pressure (sPAP) and mean pulmonary artery pressure (mPAP) (**Figure 5D-E**), indicating its potential as a biomarker. As a secreted protein, we further investigated the biological function of circulating BGN *in vitro*. Functionally, recombinant human BGN (rhBGN) enhanced hPASMC proliferation (**Figure S4L**) and viability (**Figure S4M**) compared with the negative control (bovine serum albumin, BSA). In parallel, rhBGN induced an apoptosis-resistant phenotype in hPASMCs, as evidenced by reduced cleaved caspase-3 expression (**Figure S4N**) and decreased apoptotic cell populations detected by flow cytometry (**Figure S4O**).

To evaluate the specific role of BGN in PH generation, we generated endothelial-specific BGN knockout mice (BGN^{ECKO}) (**Figure S5A**). Since BGN is located on the X chromosome, male mice carry a single floxed allele ($BGN^{f/0}$) and female mice carry two floxed alleles ($BGN^{f/f}$), and these mice are collectively referred to as BGN^{flox} mice. Notably, SuHx-induced increases in RVSP and RV/(LV+S) were significantly attenuated in BGN^{ECKO} mice compared with BGN^{flox} controls (**Figure 5F-G**). Consistently, BGN^{ECKO} mice showed reduced PAs remodeling (**Figure 5H-K**). Lung angiogram also revealed the better-preserved lung vasculature in BGN^{ECKO} mice (**Figure 5L**). Histological assessment of the RV showed a significant reduction in hypertrophy in BGN^{ECKO} mice treated with SuHx (**Figure 5M**). Echocardiography further demonstrated that SuHx-induced decreases in PAT/PET, TAPSE, RVFAC, and increases in RVFWT were less pronounced in BGN^{ECKO} mice than in BGN^{flox} mice (**Figure S5B-E**). Together, our data suggest that endothelial BGN plays an important role in PH development.

267

268 **TXNDC5 Assists BGN Protein Folding to Drive Pulmonary Hypertension**

269 To elucidate how TXNDC5 regulates BGN, we first performed Western blots to
270 validate the positive regulation of TXNDC5 on BGN both *in vitro* and *in vivo*. The
271 silencing of TXNDC5 reversed the overexpression of BGN induced by hypoxia
272 stimulation in hPAECs (**Figure S5F**). Reduced BGN expression was also observed in
273 the lungs of TXNDC5-deficient mice (**Figure S5G**), which was consistent with the
274 findings in primary lung ECs isolated from $TXNDC5^{ECKO}$ mice (**Figure S5H**). In
275 contrast, BGN expression was elevated in hPAECs following lentiviral-mediated
276 TXNDC5 overexpression (**Figure S5I**) and in primary lung ECs isolated from AAV-
277 TXN-treated mice (**Figure S5J**).

278 To further assess the direct interaction between TXNDC5 and BGN, we
279 investigated the subcellular location at which TXNDC5 binds to BGN. Immunostaining
280 assays showed that TXNDC5 colocalized with BGN (**Figure 6A**). We also performed
281 co-IP analysis and found that TXNDC5 bound to BGN, and the binding was enhanced
282 upon hypoxia exposure (**Figure 6B** and **Figure S5K**). To identify the protein domain
283 of TXNDC5 that was involved in the interaction with BGN, we performed molecular
284 docking analysis and revealed that multiple sites of TXNDC5 (Cys89, Ser125, Gly351,
285 and His352) might be involved in the interaction with BGN (**Figure 6C**). Thus, we
286 constructed four TXNDC5 mutants (C89A, S125A, G351A, and H352A) to identify
287 the residue that plays a key role in this process. Co-IP analysis showed that C89A and
288 G351A could partially abolish TXNDC5 binding with BGN (**Figure 6D**), suggesting
289 that these amino acid residues might be essential for the binding of TXNDC5 and BGN.

290 TXNDC5, an endoplasmic reticulum resident protein with three thioredoxin
291 domains containing CGHC motifs, catalyzes disulfide bond formation[14]. Thus, we
292 hypothesized that TXNDC5 facilitates the folding of BGN, enabling its maturation,
293 signaling, and secretion. To test this, we generated a PDI-inactive TXNDC5 mutant
294 (TXNDC5 Mut) with cysteine-to-alanine substitutions in all three domains (**Figure**
295 **S5L**). Fluorescence resonance energy transfer (FRET)-based protein folding assays
296 (**Figure S5M**) showed that LV-TXNDC5 increased BGN folding efficiency, whereas

297 TXNDC5 Mut did not (**Figure 6E**). Moreover, cycloheximide (CHX) chase assays
298 further demonstrated that overexpression of TXNDC5 markedly prolonged the half-life
299 of BGN (**Figure S5N**), whereas TXNDC5 silencing accelerated BGN degradation
300 (**Figure S5O**). These results indicate that TXNDC5 relies on its PDI activity to promote
301 BGN folding, stability, and extracellular secretion from hPAECs.

302 To assess whether BGN mediates the endothelial TXNDC5 *in vivo*, we
303 overexpressed TXNDC5 in lung ECs of BGN^{ECKO} and BGN^{flox} mice (**Figure 6F**). In
304 BGN^{flox} mice under SuHx conditions, AAV-TXN exacerbated distal PA muscularization,
305 medial wall thickness, and collagen deposition in BGN^{flox} mice, whereas these effects
306 were largely abolished in BGN^{ECKO} mice (**Figure 6G-J**). Consistently, AAV-TXN
307 markedly increased RVSP (**Figure 6K**) and aggravated RV hypertrophy in BGN^{flox}
308 mice, whereas both changes were significantly attenuated in BGN^{ECKO} mice (**Figure**
309 **6L**). Echocardiographic assessment revealed that AAV-TXN led to pronounced
310 deterioration of RV performance, while these adverse functional changes were largely
311 blunted in BGN^{ECKO} mice (**Figure S5P-S**). Together, these results indicate that
312 endothelial BGN is required for TXNDC5-mediated pulmonary vascular remodeling
313 and PH development, confirming BGN as a key downstream effector of TXNDC5.

314

315 **A Positive Feedback Loop Exists Between TXNDC5 and HIF Signaling**

316 HIF α subunits are the dominant effector activated by hypoxia, suggesting that HIF
317 signaling may regulate TXNDC5 transcription. qPCR analysis showed that silencing of
318 HIF-2α, but not HIF-1α, markedly downregulated TXNDC5 mRNA levels under both
319 normoxia and hypoxia conditions (**Figure S6A-B**). Western blot analysis also
320 demonstrated that the protein level of TXNDC5 was significantly decreased when HIF-
321 2α was knocked down (**Figure S6C**). Next, two putative HIF-2α binding sites (BS1 and
322 BS2) were identified in the TXNDC5 promoter (**Figure S6D**). Chromatin
323 immunoprecipitation (ChIP) assays confirmed HIF-2α binding to both sites (**Figure**
324 **S6E**), and dual-luciferase reporter assays showed that mutation of either site reduced
325 promoter activity, with mutation of both causing a further decrease (**Figure 7A**). These
326 results indicate that BS1 and BS2 synergistically mediate HIF-2α-driven TXNDC5

327 transcription. Moreover, we found that silencing TXNDC5 markedly reduced HIF-
328 1α/2α protein levels under hypoxia (**Figure S6F**), consistent with observations in the
329 lungs of TXNDC5-deficient mice (**Figure 7B**). Nuclear localization of HIF-1α/2α was
330 also decreased upon TXNDC5 knockdown, as confirmed by Western blot and
331 immunofluorescence (**Figure S6G-H**). These results indicate a positive feedback loop
332 between TXNDC5 and HIF signaling during hypoxia.

333 To assess whether HIF signaling mediates the pathogenic effects of endothelial
334 TXNDC5 *in vivo*, mice overexpressing TXNDC5 via AAV-TXN were treated with
335 selective HIF-1α (PX-478) or HIF-2α (PT-2385) inhibitors under normoxia or SuHx
336 (**Figure S6I**). As expected, AAV-TXN markedly exacerbated PH phenotypes, including
337 distal PA remodeling, increased RVSP, RV hypertrophy, and impaired RV function.
338 Importantly, HIF inhibitors significantly attenuated these TXNDC5-induced vascular
339 and cardiac abnormalities, as shown by histology (**Figure 7C-F**), hemodynamics
340 (**Figure S6J**), evaluation of RV hypertrophy (**Figure S6K**), and echocardiographic
341 analysis (**Figure S6L-O**). Collectively, these results indicate that TXNDC5 promotes
342 PH via a HIF-dependent positive feedback loop.

343

344 **TXNDC5 Requires BGN to Inhibit the Ubiquitination of HIF-1α/2α**

345 Interestingly, we found in the present study that the HIF-1α/2α protein levels were
346 significantly decreased by the silencing of BGN upon hypoxia exposure in hPAECs
347 (**Figure S7A**). Since TXNDC5 directly interacted with BGN, we hypothesized that the
348 regulation of HIF-1α/2α by TXNDC5 required the presence of BGN. Western blots
349 revealed that LV-TXNDC5 increased the expression of HIF-1α/2α both under normoxic
350 and hypoxic conditions in hPAECs (**Figure S7B**). More importantly, knockdown of
351 BGN abolished the upregulation of HIF-1α/2α induced by LV-TXNDC5 (**Figure 7G**).
352 These data suggest that TXNDC5 requires BGN to regulate the HIF signaling pathway.

353 Under normoxia, HIF-α is rapidly ubiquitinated by E3 ligase von Hippel-Lindau
354 (VHL) and degraded[22]. Notably, TXNDC5 overexpression increased the HIF-1α/2α
355 levels even under normoxic conditions, which was also observed in primary lung ECs
356 from AAV-TXN-treated mice (**Figure S7C**). CHX chase assays showed that TXNDC5

prolonged the half-life of HIF-1α/2α in hPAECs (**Figure 7H** and **Figure S7D**). Mechanistically, TXNDC5 silencing increased VHL expression, while concurrent knockdown of VHL rescued the reduction of HIF-1α/2α caused by TXNDC5 depletion under hypoxia (**Figure 7I**). *In vivo* ubiquitination assays further revealed that TXNDC5 overexpression suppressed HIF-1α/2α ubiquitination, whereas BGN silencing enhanced ubiquitination by upregulating VHL. Importantly, BGN knockdown abolished the TXNDC5-induced inhibition of HIF-1α/2α ubiquitination and VHL downregulation (**Figure 7J** and **Figure S7E**). Collectively, these results demonstrate that TXNDC5 stabilizes HIF-1α/2α by inhibiting VHL-mediated ubiquitination in a BGN-dependent manner.

E64FC26 Exhibits Therapeutic Effects Against PH in Rats

E64FC26 is a potent PDI pan-inhibitor, with IC_{50} of 16.3 μM against TXNDC5[23]. To evaluate the toxicity and safety of E64FC26, we performed histological analyses on the major organs of rats continuously treated with E64FC26 for 5 weeks under normoxic conditions. In the kidneys, the renal tubules and glomeruli maintained their integrity, with no signs of tubular dilation, epithelial cell injury, necrosis, or noticeable inflammatory cell infiltration in the kidneys. Similarly, hepatocytes were well-organized with clear cell boundaries, and there were no indications of necrosis, cell swelling, or inflammatory cell infiltration in the liver. Histological examination of the spleen revealed intact white and red pulp structures, without evidence of lymphoid depletion, congestion, or inflammatory infiltration (**Figure S8A**). Furthermore, body weight measurements showed no significant differences after E64FC26 treatment compared with the vehicle (**Figure S8B**). These findings collectively indicate that E64FC26 exhibits a favorable safety profile without causing overt organ or systemic toxicity.

Then, to examine whether pharmacological inhibition of TXNDC5 activity produces a therapeutic effect on PH, E64FC26 was administered intraperitoneally in SuHx-induced PH rats (**Figure 8A**). Hemodynamic measurements and morphometric analysis demonstrated that E64FC26 administration attenuated the elevation of RVSP

(**Figure 8B**) and the increase in RV/(LV+S) ratio (**Figure 8C**) in SuHx-induced PH rats compared with those with vehicle treatment. Histological analyses revealed that E64FC26 reversed SuHx-induced PA remodeling compared with vehicle-treated rats, as evidenced by reduced distal PA muscularization, decreased medial wall thickness, and attenuated collagen deposition area (**Figure 8D** and **Figure S8C-E**). Echocardiographic assessment further indicated that E64FC26 alleviated RV dysfunction in SuHx-induced PH rats (**Figure S8F**). Consistent with the echocardiographic improvements, histological analyses revealed that E64FC26 administration significantly reversed the RV hypertrophy (**Figure 8E**) and reduced the RV fibrosis area (**Figure 8F**) in SuHx-induced PH rats compared with those treated with vehicle.

To assess whether the therapeutic effects of E64FC26 in PH *in vivo* are primarily mediated through TXNDC5 rather than off-target inhibition of other PDI family members, we treated TXNDC5^{ECKO} mice with E64FC26 under SuHx conditions (**Figure 8G**). Notably, E64FC26 treatment also exhibited therapeutic effects in TXNDC5$^{f/f}$ mice against SuHx challenged, consistent with the results observed in rats. More importantly, in TXNDC5 endothelial-deficient mice, administration of E64FC26 did not confer additional protection against SuHx-induced distal PA remodeling, as indicated by unchanged medial wall thickness and collagen deposition area compared with vehicle-treated TXNDC5^{ECKO} mice (**Figure 8H** and **Figure S8G-H**). Similarly, lung angiography showed that E64FC26 administration failed to improve distal pulmonary perfusion in SuHx-treated TXNDC5^{ECKO} mice (**Figure 8I**). Consistently, E64FC26 also did not attenuate RVSP elevation (**Figure S8I**), RV hypertrophy (**Figure S8J**), and RV functional impairment (**Figure S8K**) in these mice. These findings indicated that the therapeutic effect of E64FC26 in PH would be largely dependent on the targeting of endothelial TXNDC5 rather than off-target inhibition of other PDI family members. In a word, these results indicate that pharmacological inhibition of TXNDC5 activity may be a promising strategy to alleviate the progression of PH.

Pulmonary Endothelium-Targeted TXNDC5 Gene Therapy Ameliorates PH

We further established a pulmonary endothelium-targeted gene therapy approach to enhance organ specificity. Using a self-complementary adeno-associated virus (scAAV) vector encoding shRNA against TXNDC5 (shTXN), we achieve rapid and endothelial-specific gene silencing *in vivo*. The vector was administered via the tail vein to SuHx-induced PH rats to selectively suppress TXNDC5 in lung ECs and evaluate its therapeutic efficacy (**Figure 8J**). *Ex vivo* imaging confirmed efficient lung targeting of the AAV (**Figure 8K**), and Western blotting demonstrated marked suppression of TXNDC5 expression in primary rat lung ECs (**Figure S8L**).

Treatment with shTXN significantly attenuated SuHx-induced PA remodeling compared with rats receiving the control vector (shNC), as evidenced by reduced distal PA muscularization, decreased medial wall thickness, and lower collagen deposition area (**Figure 8L** and **Figure S8M-O**). Hemodynamic measurements further demonstrated that shTXN administration attenuated the elevation of RVSP in SuHx-induced PH rats (**Figure 8M**). Moreover, morphological and histological analyses showed that shTXN decreased the RV/(LV+S) ratio (**Figure S8P**) and alleviated RV wall thickening (**Figure 8N**). Consistently, echocardiographic assessment revealed improved RV function, reflected by increased PAT/PET, TAPSE, RVFAC, and reduced RVFWT (**Figure S8Q**). These findings demonstrate that endothelial-targeted TXNDC5 silencing effectively mitigates pulmonary vascular remodeling and right heart dysfunction in PH. Collectively, these findings demonstrate that endothelial-targeted TXNDC5 silencing effectively mitigates pulmonary vascular remodeling and right heart dysfunction in PH, highlighting the therapeutic potential of TXNDC5 inhibition.

DISCUSSION

PDI family catalyzes disulfide bond formation and rearrangement in the endoplasmic reticulum. Using 4D label-free proteomics, we identified TXNDC5 as the most significantly dysregulated PDI family member in the lungs of patients with hypoxic PH. TXNDC5, dominantly expressed in endothelial cells, was also known as endothelial PDI (Endo-PDI)[24]. We found that the silencing of TXNDC5 inhibited the

446 proliferation and migration of hPAECs, whereas its overexpression led to changes in
447 the cytoskeletal architecture of hPAECs, implying a critical role of TXNDC5 in
448 endothelial dysfunction in PH. *In vivo*, global or endothelial-specific TXNDC5 deletion
449 attenuated, while endothelial TXNDC5 overexpression exacerbated SuHx-induced PH.
450 Pharmacological inhibition with E64FC26, a pan-PDI inhibitor with an IC50 of 16.3
451 μM against TXNDC5, alleviated pulmonary arterial remodeling and right ventricular
452 hypertrophy, thereby preventing PH progression in rats. These findings identify
453 TXNDC5 as a promising therapeutic target for PH.

454 We next examined the molecular mechanisms of the critical role of TXNDC5 in
455 PH development. Accumulating evidence indicates that ECM remodeling, which
456 precedes pulmonary vascular remodeling, is a key driver of PH progression by altering
457 vascular stiffness and resistance[25]. In this study, we identified TXNDC5 as a central
458 regulator of ECM homeostasis in hypoxic PH. TXNDC5 broadly modulated ECM
459 components, including proteoglycans and glycoproteins that govern matrix stiffness
460 and elasticity, collagens that provide structural support, matrix modulators and adhesion
461 proteins involved in ECM crosslinking, and metallopeptidases responsible for ECM
462 turnover. TXNDC5 also influenced basement membrane proteins and angiogenesis-
463 related factors, thereby affecting endothelial barrier function and vascular homeostasis.
464 Notably, excessive deposition of POSTN, BGN, LOX, and TGM2 was observed in the
465 PAs of SuHx-treated $TXNDC5^{f/f}$ mice but was markedly reduced in $TXNDC5^{ECKO}$ mice.
466 As key ECM regulators, POSTN and BGN promote matrix organization and
467 mechanotransduction[26–28], whereas LOX and TGM2 facilitate ECM crosslinking and
468 collagen stabilization[29,30], collectively driving vascular stiffening and remodeling.
469 These findings imply that TXNDC5 inhibition shifts the ECM equilibrium toward a
470 less fibrotic and more compliant phenotype, mitigating PH progression by preserving
471 vascular ECM homeostasis.

472 BGN has been implicated in inflammation, metabolic, musculoskeletal, and
473 oncogenic diseases[31]. In the present study, we identified BGN as a direct binding partner
474 of TXNDC5, with enhanced interaction with hypoxia exposure. Mutations at Cys89

475 and Gly351 within the PDI active domains of TXNDC5 markedly disrupted TXNDC5–
476 BGN binding, indicating that PDI activity is essential for this interaction. Consistently,
477 WT-TXNDC5, but not the PDI-inactive mutant, significantly increased FRET
478 efficiency in the BGN folding assay, demonstrating that TXNDC5 facilitates BGN
479 folding in a PDI-dependent manner. This process is critical for BGN maturation,
480 stability, and secretion. Further investigation revealed that BGN was upregulated in the
481 lungs of PH patients and rodent models. Endothelial cell-specific deficiency of BGN
482 significantly alleviated PH progression in mice, highlighting endothelial-derived BGN
483 as a key contributor to disease pathogenesis. Importantly, BGN deficiency largely
484 abolished TXNDC5 overexpression-induced distal PA remodeling and RV hypertrophy,
485 establishing BGN as a critical downstream effector of TXNDC5-driven PH. Notably,
486 serum BGN levels were significantly elevated in PH patients and strongly correlated
487 with disease severity, suggesting that BGN may serve as a potential diagnostic
488 biomarker for PH.

489 HIF signaling is a central driver of hypoxic PH, with HIF-α subunits rapidly
490 degraded under normoxia via the VHL E3 ligase[32,33]. In this study, we showed that
491 TXNDC5-induced upregulation of HIF-1α/2α depends on BGN, as endothelial BGN
492 silencing restored VHL-mediated ubiquitination and degradation of HIF-1α/2α. These
493 findings uncover a previously unrecognized mechanism linking ECM remodeling to
494 hypoxia-driven signaling in PH and suggest that TXNDC5, BGN, and HIF form a
495 coordinated regulatory axis during disease progression. Excessive systemic inhibition
496 of HIF-1α or HIF-2α has been associated with organ dysfunction, developmental
497 defects, and embryonic lethality in mice, highlighting safety concerns for direct HIF
498 targeting.[34–36]. We found that global TXNDC5 deletion prevented SuHx-induced HIF
499 activation without causing adverse effects on growth or organ development. These
500 findings suggest that targeting TXNDC5 offers a more tissue-selective strategy to
501 modulate pathological HIF signaling while minimizing systemic toxicity, providing a
502 promising therapeutic alternative for PH.

503 In summary, we identified for the first time the novel role of PDI protein TXNDC5

in the pathogenesis of hypoxic PH. TXNDC5 facilitates ECM protein (e.g., BGN) folding and reduces HIF-1α/2α ubiquitination, which contributes to endothelial dysfunction. TXNDC5 promotes a positive feedback loop between BGN and HIF signaling, driving the progression of pulmonary vascular remodeling in PH. This study highlights TXNDC5 as a promising therapeutic target for hypoxia-induced PH and lays the groundwork for future clinical investigations.

Acknowledgments

We thank Professor John Shyy from the University of California, San Diego, United States, for critical reading and advice on this article.

Sources of Funding

This work was supported by the Key Program of National Natural Science Foundation of China (NSFC, grant No. 82430004 to Jin-Song Bian), Shenzhen Science Fund for Distinguished Young Scholars (grant No. RCJC20210706091946002 to Xiaowei Nie), Shenzhen Science and Technology Program (grant No. GJHZ20240218111401002 to Jin-Song Bian), the National Natural Science Foundation of China (NSFC, grant No. 82241021 to Xiaowei Nie), and the National Natural Science Foundation of China (NSFC, grant No. 82400063 to Junting Zhang).

References

1. Johnson S, Sommer N, Cox-Flaherty K, Weissmann N, Ventetuolo CE, Maron BA. Pulmonary Hypertension: A Contemporary Review. *Am J Respir Crit Care Med*. 2023;208:528–548.

2. Shlobin OA, Adir Y, Barbera JA, Cottin V, Harari S, Jutant E-M, Pepke-Zaba J, Ghofrani H-A, Channick R. Pulmonary hypertension associated with lung diseases. *Eur Respir J*. 2024;64:2401200.

3. Evans CE, Cober ND, Dai Z, Stewart DJ, Zhao Y-Y. Endothelial cells in the pathogenesis of pulmonary arterial hypertension. *Eur Respir J*. 2021;58:2003957.

4. Ma B, Cao Y, Qin J, Chen Z, Hu G, Li Q. Pulmonary artery smooth muscle cell

534 phenotypic switching: A key event in the early stage of pulmonary artery
535 hypertension. *Drug Discov Today*. 2023;28:103559.

536 5. Mandras SA, Mehta HS, Vaidya A. Pulmonary Hypertension: A Brief Guide for
537 Clinicians. *Mayo Clin Proc*. 2020;95:1978–1988.

538 6. Olsson KM, Corte TJ, Kamp JC, Montani D, Nathan SD, Neubert L, Price LC,
539 Kiely DG. Pulmonary hypertension associated with lung disease: new insights
540 into pathomechanisms, diagnosis, and management. *Lancet Respir Med*.
541 2023;11:820–835.

542 7. Kanemura S, Matsusaki M, Inaba K, Okumura M. PDI Family Members as Guides
543 for Client Folding and Assembly. *Int J Mol Sci*. 2020;21:9351.

544 8. Kuramochi T, Yamashita Y, Arai K, Kanemura S, Muraoka T, Okumura M.
545 Boosting the enzymatic activity of CxxC motif-containing PDI family members.
546 *Chem Commun (Camb)*. 2024;60:6134–6137.

547 9. Nagarkoti S, Kim Y-M, Ash D, Das A, Vitriol E, Read T-A, Youn S-W, Sudhahar
548 V, McMenamin M, Hou Y, et al. Protein disulfide isomerase A1 as a novel redox
549 sensor in VEGFR2 signaling and angiogenesis. *Angiogenesis*. 2023;26:77–96.

550 10. Kobayashi Y, Oguro A, Hirata Y, Imaoka S. The regulation of Hypoxia-Inducible
551 Factor-1 (HIF-1alpha) expression by Protein Disulfide Isomerase (PDI). *PLoS*
552 *One*. 2021;16:e0246531.

553 11. Hung C-T, Tsai Y-W, Wu Y-S, Yeh C-F, Yang K-C. The novel role of ER protein
554 TXNDC5 in the pathogenesis of organ fibrosis: mechanistic insights and
555 therapeutic implications. *J Biomed Sci*. 2022;29:63.

556 12. Jin Y, Sharma A, Bai S, Davis C, Liu H, Hopkins D, Barriga K, Rewers M, She J-
557 X. Risk of type 1 diabetes progression in islet autoantibody-positive children can
558 be further stratified using expression patterns of multiple genes implicated in
559 peripheral blood lymphocyte activation and function. *Diabetes*. 2014;63:2506–
560 2515.

561 13. Wang L, Dong H, Song G, Zhang R, Pan J, Han J. TXNDC5 synergizes with
562 HSC70 to exacerbate the inflammatory phenotype of synovial fibroblasts in
563 rheumatoid arthritis through NF-κB signaling. *Cell Mol Immunol*. 2018;15:685–
564 696.

565 14. Wang X, Li H, Chang X. The role and mechanism of TXNDC5 in diseases. *Eur J*
566 *Med Res*. 2022;27:145.

567 15. Yeh C-F, Cheng S-H, Lin Y-S, Shentu T-P, Huang R-T, Zhu J, Chen Y-T, Kumar
568 S, Lin M-S, Kao H-L, et al. Targeting mechanosensitive endothelial TXNDC5 to
569 stabilize eNOS and reduce atherosclerosis in vivo. *Sci Adv*. 2022;8:eabl8096.

570 16. Wu S, Luo X, Chen Y, Wang Z, Liu X, Sun N, Zhao J, Luo W, Zhang J, Tong X,
571 et al. Sodium-glucose cotransporter 2 inhibitors attenuate vascular calcification by
572 suppressing endoplasmic reticulum protein thioredoxin domain containing 5
573 dependent osteogenic reprogramming. *Redox Biol*. 2024;73:103183.

574 17. Fu Y, Zhou Y, Wang K, Li Z, Kong W. Extracellular Matrix Interactome in
575 Modulating Vascular Homeostasis and Remodeling. *Circ Res*. 2024;134:931–949.

576 18. Thenappan T, Chan SY, Weir EK. Role of extracellular matrix in the pathogenesis
577 of pulmonary arterial hypertension. *Am J Physiol Heart Circ Physiol*.
578 2018;315:H1322–H1331.

579 19. Nie X, Shen C, Tan J, Wu Z, Wang W, Chen Y, Dai Y, Yang X, Ye S, Chen J, et al.
580 Periostin: A Potential Therapeutic Target For Pulmonary Hypertension? *Circ Res*.
581 2020;127:1138–1152.

582 20. Bian J-S, Chen J, Zhang J, Tan J, Chen Y, Yang X, Li Y, Deng L, Chen R, Nie X.
583 ErbB3 Governs Endothelial Dysfunction in Hypoxia-Induced Pulmonary
584 Hypertension. *Circulation*. 2024;150:1533–1553.

585 21. Zhang Y, Li X, Li S, Zhou Y, Zhang T, Sun L. Immunotherapy for Pulmonary
586 Arterial Hypertension: From the Pathogenesis to Clinical Management. *Int J Mol*
587 *Sci*. 2024;25:8427.

588 22. Luo Z, Tian M, Yang G, Tan Q, Chen Y, Li G, Zhang Q, Li Y, Wan P, Wu J.
589 Hypoxia signaling in human health and diseases: implications and prospects for
590 therapeutics. *Signal Transduct Target Ther*. 2022;7:218.

591 23. Robinson RM, Reyes L, Duncan RM, Bian H, Reitz AB, Manevich Y, McClure
592 JJ, Champion MM, Chou CJ, Sharik ME, et al. Inhibitors of the protein disulfide
593 isomerase family for the treatment of multiple myeloma. *Leukemia*.
594 2019;33:1011–1022.

595 24. Sullivan DC, Huminiecki L, Moore JW, Boyle JJ, Poulsom R, Creamer D, Barker
596 J, Bicknell R. EndoPDI, a novel protein-disulfide isomerase-like protein that is
597 preferentially expressed in endothelial cells acts as a stress survival factor. *J Biol*
598 *Chem*. 2003;278:47079–47088.

599 25. Jandl K, Radic N, Zeder K, Kovacs G, Kwapiszewska G. Pulmonary vascular
600 fibrosis in pulmonary hypertension - The role of the extracellular matrix as a
601 therapeutic target. *Pharmacol Ther*. 2023;247:108438.

602 26. Sun X-J, Ma W-Q, Zhu Y, Liu N-F. POSTN promotes diabetic vascular
603 calcification by interfering with autophagic flux. *Cell Signal*. 2021;83:109983.

604 27. Nikoloudaki G, Snider P, Simmons O, Conway SJ, Hamilton DW. Periostin and
605 matrix stiffness combine to regulate myofibroblast differentiation and fibronectin

606 synthesis during palatal healing. *Matrix Biol*. 2020;94:31–56.

607 28. Yu M, He X, Song X, Gao J, Pan J, Zhou T, Wang Q, Zhu W, Ma H, Zeng H, et al.
608 Biglycan promotes hepatic fibrosis through activating heat shock protein 47. *Liver*
609 *Int*. 2023;43:500–512.

610 29. Wang Z-J, Guan Q-W, Zhou H-H, Mao X-Y, Chen F-H. Mechanistic insight into
611 lysyl oxidase in vascular remodeling and angiogenesis. *Genes Dis*. 2023;10:771–
612 785.

613 30. Zhang M, Li L, Zhang W, Li M, Yan G, Tang C. TG2 participates in pulmonary
614 vascular remodelling by regulating the senescence of pulmonary artery smooth
615 muscle cells. *Cell Signal*. 2024;121:111296.

616 31. Appunni S, Rubens M, Ramamoorthy V, Anand V, Khandelwal M, Sharma A.
617 Biglycan: an emerging small leucine-rich proteoglycan (SLRP) marker and its
618 clinicopathological significance. *Mol Cell Biochem*. 2021;476:3935–3950.

619 32. Tarade D, Ohh M. The HIF and other quandaries in VHL disease. *Oncogene*.
620 2018;37:139–147.

621 33. Pullamsetti SS, Mamazhakypov A, Weissmann N, Seeger W, Savai R. Hypoxia-
622 inducible factor signaling in pulmonary hypertension. *J Clin Invest*.
623 2020;130:5638–5651.

624 34. Kotch LE, Iyer NV, Laughner E, Semenza GL. Defective vascularization of HIF-
625 1alpha-null embryos is not associated with VEGF deficiency but with
626 mesenchymal cell death. *Dev Biol*. 1999;209:254–267.

627 35. Chen H, Houshmand G, Mishra S, Fong G-H, Gittes GK, Esni F. Impaired
628 pancreatic development in Hif2-alpha deficient mice. *Biochem Biophys Res*
629 *Commun*. 2010;399:440–445.

630 36. Peng Y-J, Nanduri J, Khan SA, Yuan G, Wang N, Kinsman B, Vaddi DR, Kumar
631 GK, Garcia JA, Semenza GL, et al. Hypoxia-inducible factor 2α (HIF-2α)
632 heterozygous-null mice exhibit exaggerated carotid body sensitivity to hypoxia,
633 breathing instability, and hypertension. *Proc Natl Acad Sci U S A*. 2011;108:3065–
634 3070.

635

636

637 **Figure legends**

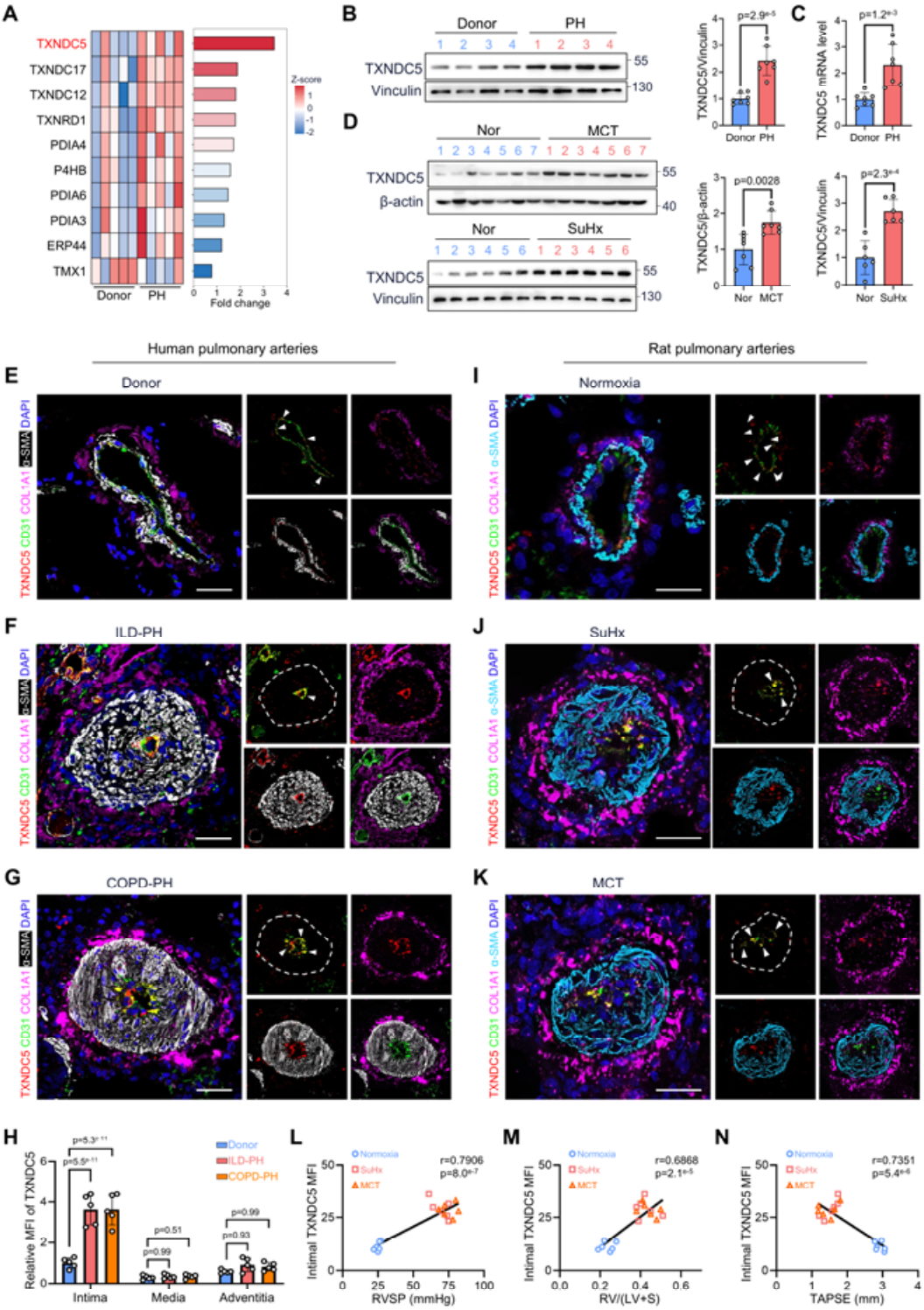

638

639 **Figure 1. TXNDC5 was upregulated in PH.**

640 **A**, Heatmap of 4D label-free proteomics showing PDI family expression in lung tissues

641 from 5 non-PH donors and 5 patients with hypoxic PH. **B**, Representative Western blots
642 and quantification of TXNDC5 and Vinculin in the lungs of control donors and PH
643 patients (n=7). **C**, qPCR analysis of TXNDC5 mRNA levels in lung homogenates from
644 donors and patients with PH (n=7). **D**, Western blots showing the TXNDC5 protein
645 levels in the lungs collected from MCT (n=7) or SuHx-treated rats (n=6) or rats under
646 normoxia. **E**, **F**, and **G**, Representative confocal images of multiplex
647 immunofluorescence (mIF) staining for TXNDC5 (red), CD31 (green), α-SMA (white),
648 and COL1A1 (purple) in distal pulmonary arteries (PAs) from donors, ILD-PH, and
649 COPD-PH patients. Nuclei were counterstained with DAPI (blue). White arrows
650 indicate the colocalization of TXNDC5 with CD31 (yellow). White dashed lines
651 indicate the outer layer of smooth muscle cells. Scale bars=25 μm. **H**, Quantitative
652 analysis showing elevated TXNDC5 mean fluorescence intensity (MFI) in the $CD31^+$
653 intima of distal PAs from patients with ILD-PH and COPD-PH compared with non-PH
654 donors. (n=5). **I**, **J**, and **K**, Representative images of mIF staining for TXNDC5 (red),
655 CD31 (green), α-SMA (cyan), and COL1A1 (purple) in distal PAs from SuHx- or
656 MCT-treated rats or rats under normoxia. Nuclei were counterstained with DAPI (blue).
657 White arrows indicate the colocalization of TXNDC5 with CD31 (yellow). White
658 dashed lines indicate the outer layer of smooth muscle cells. Scale bars=20 μm. **L**, **M**,
659 and **N**, Correlation analyses of intimal TXNDC5 MFI and right ventricular systolic
660 pressure (RVSP), Fulton index [RV/(LV+S)], and tricuspid annular plane systolic
661 excursion (TAPSE) in rats. Data represent the mean±SD. Comparisons of parameters
662 were performed with the unpaired 2-tailed Student *t*-test (**B-D**) or 2-way ANOVA (**H**),
663 followed by Tukey honestly significant difference test for multiple comparisons and the
664 Pearson correlation test (**L-N**). PDI indicates protein disulfide isomerase; PH,
665 pulmonary hypertension; TXNDC5, thioredoxin domain containing 5; α-SMA, α-
666 smooth muscle actin; COL1A1, collagen type I alpha 1; DAPI, 4′,6-diamidino-2-
667 phenylindole; Nor, normoxia; SuHx, Sugen5416/hypoxia; and MCT, monocrotaline.

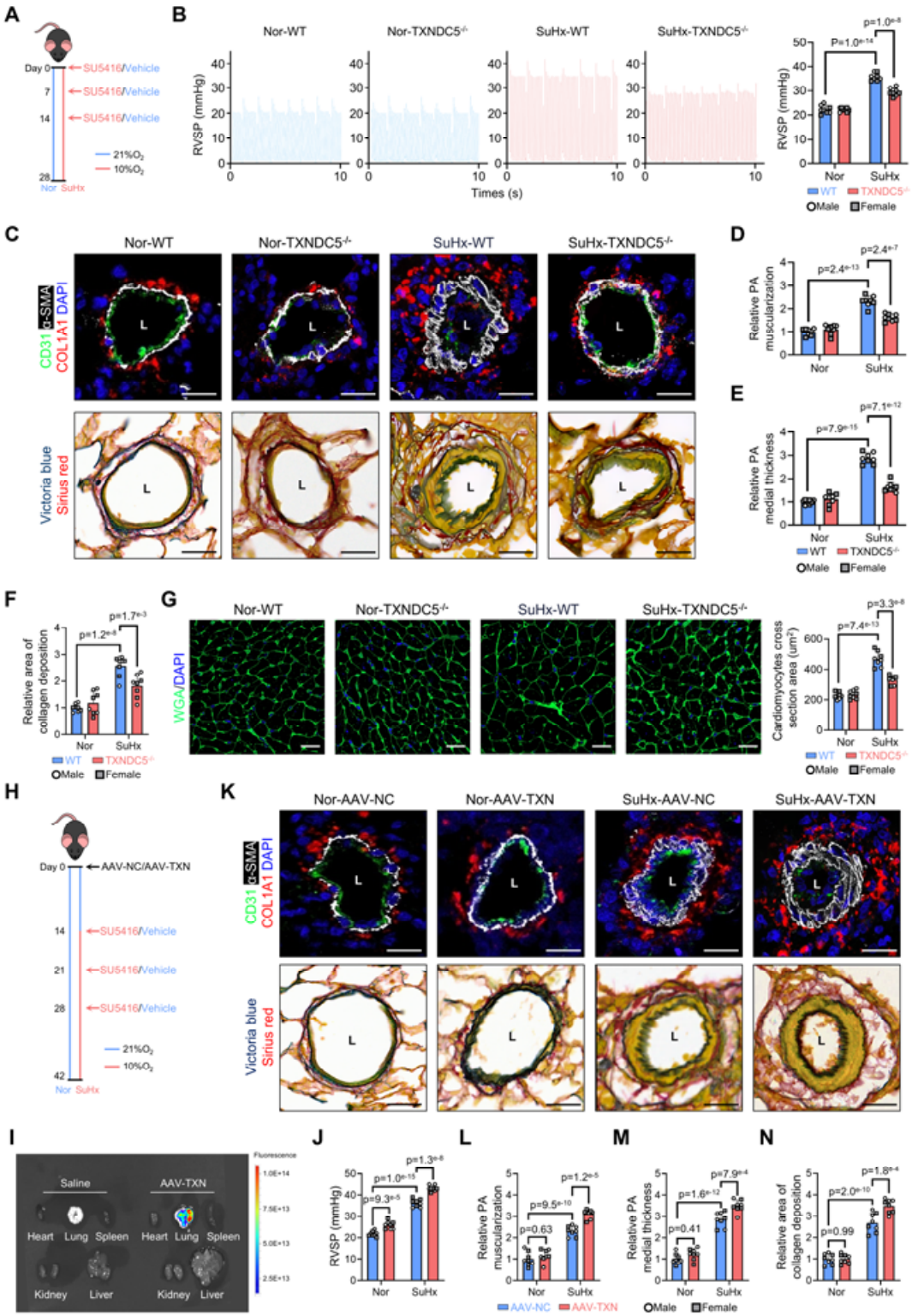

Figure 2. TXNDC5 contributed to SuHx-induced pulmonary vascular remodeling

A, Schematic protocol for the animal treatments in the SuHx-induced PH mice. **B**, Representative tracings and quantification of right ventricular systolic pressure (RVSP) in WT and TXNDC5$^{-/-}$ mice exposed to normoxia or SuHx (n=8). **C**, Representative

673 multiplex immunofluorescence (mIF) for CD31 (green), α-SMA (white), and COL1A1
674 (red), and Victoria blue/Sirius red (VB/SR) staining for elastic lamina (dark blue),
675 collagens (red), and muscle fiber (yellow) in distal pulmonary arteries (PAs) from WT
676 and TXNDC5$^{-/-}$ mice exposed to normoxia or SuHx. Nuclei were counterstained with
677 DAPI (blue). L indicates lumen. Scale bars=25 μm. **D**, Quantification of distal PA
678 muscularization based on α-SMA positive area in WT and TXNDC5$^{-/-}$ mice exposed to
679 normoxia or SuHx (n=8). **E**, Measurement of medial wall thickness in distal PAs,
680 defined by the elastic lamina visualized with VB staining (n=8). **F**, Quantification of
681 collagen deposition area in distal PAs based on SR staining, indicating decreased
682 collagen deposition in TXNDC5-deficient mice (n=8). **G**, Immunofluorescence
683 staining of WGA (green) in right ventricles from WT and TXNDC5$^{-/-}$ mice exposed to
684 normoxia or SuHx (n=8). Nuclei were counterstained with DAPI (blue). Scale bars=20
685 μm. **H**, Schematic diagram illustrating the *in vivo* pulmonary endothelial-specific
686 overexpression of TXNDC5 in mice. Mice received a single tail vein injection of AAV-
687 NC or AAV-TXN at the beginning of the 2 weeks, followed by SuHx exposure. **I**,
688 Representative images of major organs from saline-treated control or AAV-TXN-
689 treated mice, showing GFP fluorescence delivered by AAV detected by IVIS imaging
690 system. **J**, Hemodynamic measurements of RVSP in mice administered with AAV-NC
691 or AAV-TXN under normoxia or SuHx situations (n=8). **K**, Representative mIF of distal
692 PAs from AAV-NC or AAV-TXN-treated mice under SuHx or normoxia, showing CD31
693 (green), α-SMA (white), and COL1A1 (red), together with VB/SR staining of elastic
694 lamina (dark blue), perivascular collagens (red), and muscle fiber (yellow). Nuclei were
695 counterstained with DAPI (blue). L indicates lumen. Scale bars=25 μm. **L**, **M,** and **N**,
696 Quantitative analysis of distal PA remodeling in AAV-NC or AAV-TXN-treated mice
697 under normoxic or SuHx conditions (n=8). PA muscularization, medial wall thickness,
698 and collagen deposition area were assessed using α-SMA, VB, and SR staining,
699 respectively. Data represent the mean±SD. Comparisons of parameters were performed
700 with 2-way ANOVA, followed by Tukey honestly significant difference test for
701 multiple comparisons. DAPI indicates 4′,6-diamidino-2-phenylindole; α-SMA, α-
702 smooth muscle actin; COL1A1, collagen type I alpha 1; WGA, wheat germ agglutinin;

703 GFP, green fluorescent protein; Nor, normoxia; SuHx, and Sugen5416/hypoxia.

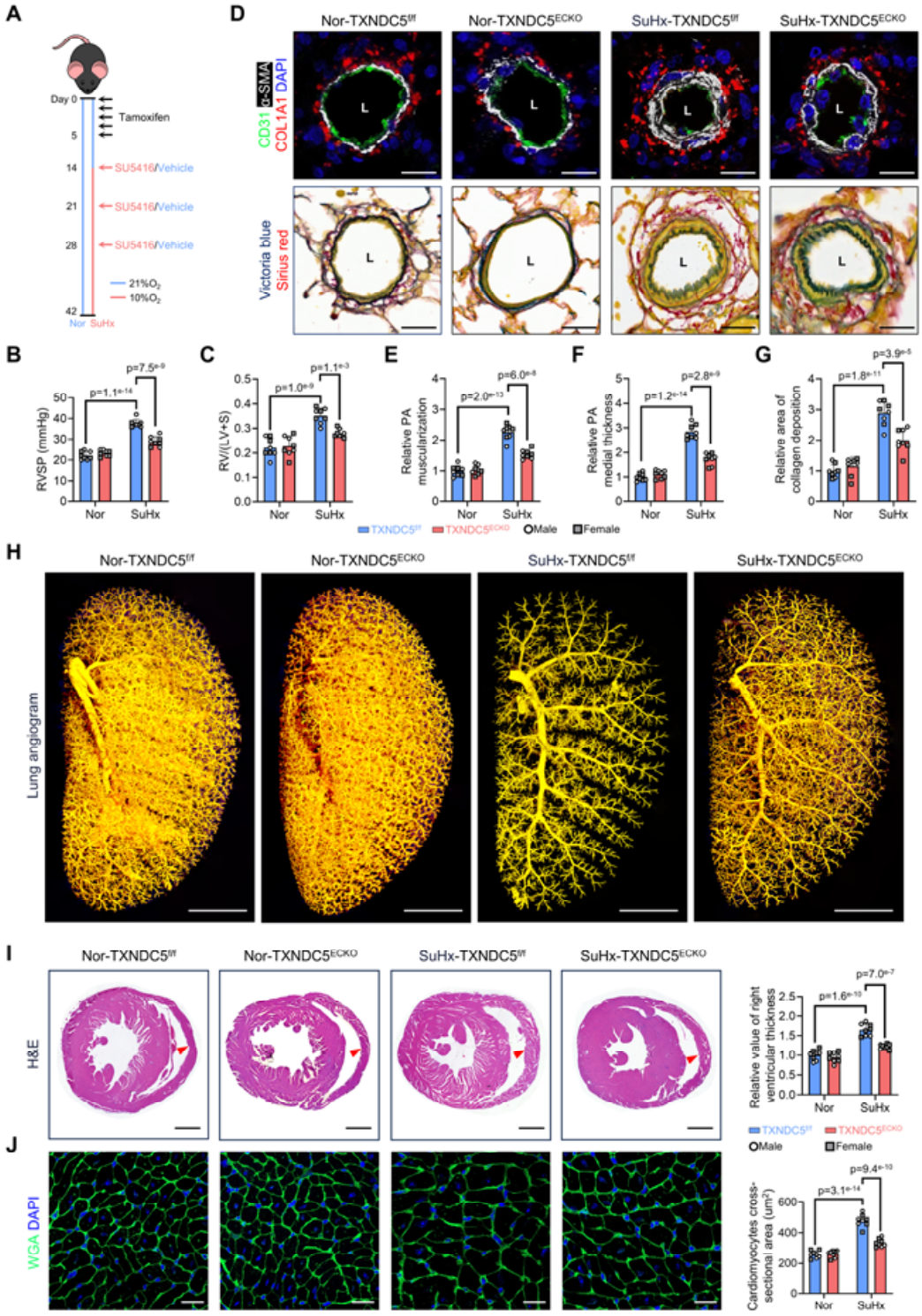

704

705 **Figure 3. Endothelial cell-specific deletion of TXNDC5 ameliorated SuHx-induced**

706 **PH.**

707 **A**, Schematic protocol for the endothelial cell-specific TXNDC5 knockout mice assays.

Mice were intraperitoneally injected with 75 mg/kg tamoxifen once daily for 5 days before being exposed to SuHx. **B**, Hemodynamic measurements of right ventricular systolic pressure (RVSP) in TXNDC5$^{f/f}$ and TXNDC5^{ECKO} mice exposed to normoxia or SuHx (n=8). **C**, Fulton index [RV/(LV+S)] in TXNDC5$^{f/f}$ and TXNDC5^{ECKO} mice (n=8). **D**, Representative multiplex immunofluorescence (mIF) of distal pulmonary arteries (PAs) from TXNDC5$^{f/f}$ and TXNDC5^{ECKO} mice under normoxia or SuHx, showing CD31 (green), α-SMA (white), and COL1A1 (red), together with Victoria blue/Sirius red (VB/SR) staining of elastic lamina (dark blue), perivascular collagens (red), and muscle fiber (yellow). Nuclei were counterstained with DAPI (blue). L indicates lumen. Scale bars=25 μm. **E**, Quantification of distal PA muscularization based on α-SMA positive area (n=8). **F**, Medial wall thickness of distal PAs, measured across the elastic lamina visualized by VB staining (n=8). **G**, Perivascular collagen deposition quantified using SR staining (n=8). **H**, Representative lung angiogram of the left lungs from TXNDC5$^{f/f}$ and TXNDC5^{ECKO} mice treated with SuHx or under normoxic conditions. Scale bars=2 mm. **I**, Histological analysis of the cross-sectioned heart at the mid-RV (red arrows) plane from TXNDC5$^{f/f}$ and TXNDC5^{ECKO} mice with or without SuHx exposure (n=8). Scale bars=1 mm. **J**, Immunofluorescence staining of WGA (green) in RV from TXNDC5$^{f/f}$ and TXNDC5^{ECKO} mice exposed to normoxia or SuHx (n=8). Nuclei were counterstained with DAPI (blue). Scale bars=20 μm. Data represent the mean±SD. Comparisons of parameters were performed with 2-way ANOVA, followed by Tukey honestly significant difference test for multiple comparisons. DAPI indicates 4′,6-diamidino-2-phenylindole; H&E, hematoxylin-eosin; α-SMA, α-smooth muscle actin; COL1A1, collagen type I alpha 1; WGA, wheat germ agglutinin; f/f, flox/flox; Nor, normoxia; SuHx, Sugen5416/hypoxia; and RV, right ventricle.

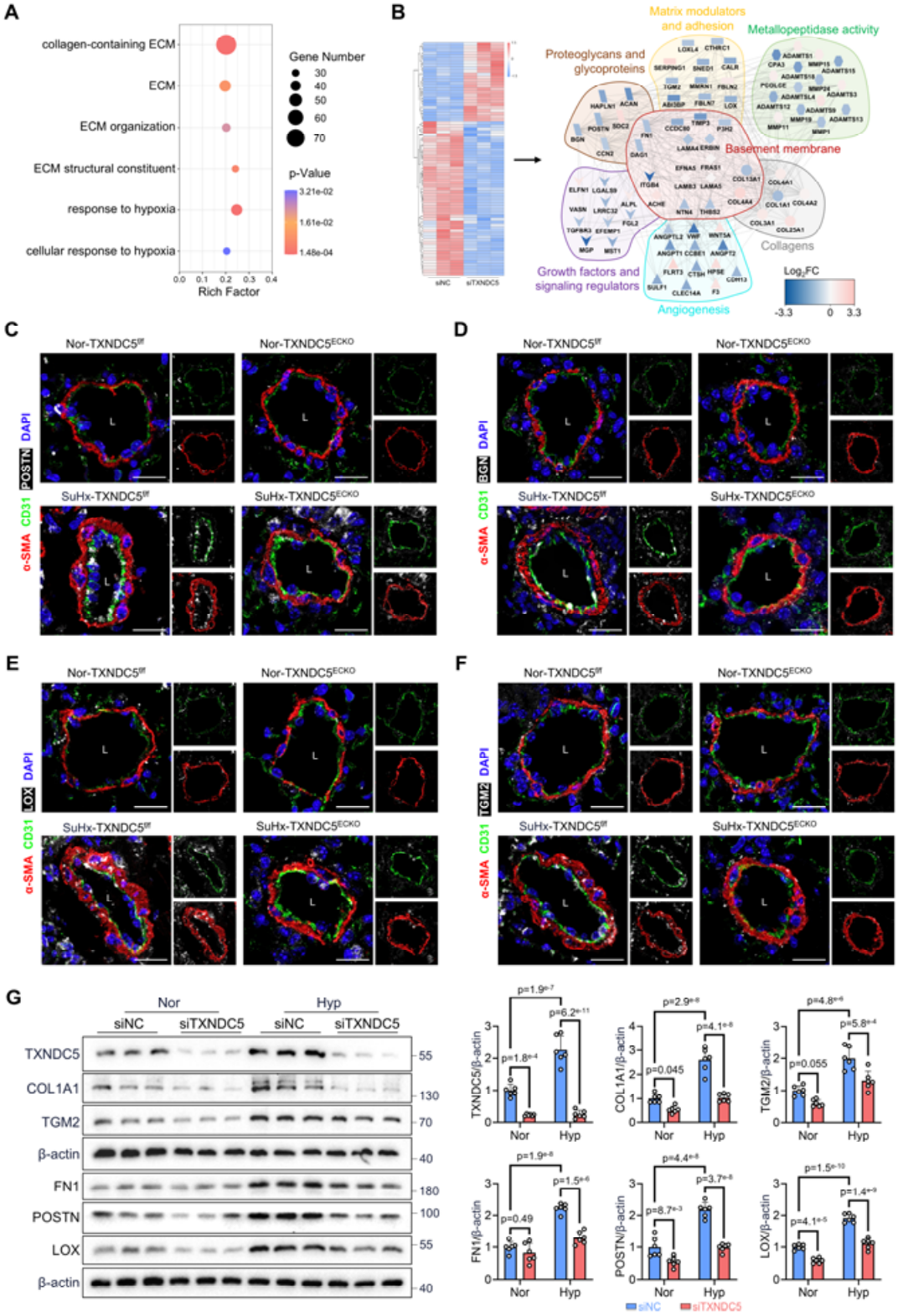

Figure 4. TXNDC5 regulated ECM protein expression and distribution.

A, HPAECs were transfected with siTXNDC5 or siNC under hypoxic conditions, followed by RNA sequencing analysis (n=3). Bubble chart showing the Gene Ontology enrichment using DAVID for the differentially expressed genes. **B**, Differentially

expressed ECM proteins were selected and visualized by heatmap (left). The PPI network showed that TXNDC5-targeted ECM proteins could be classified into different functional subgroups (right). **C**, **D**, **E**, and **F**, Representative images of immunofluorescence staining of α-SMA (red), CD31 (green), and POSTN, BGN, LOX, or TGM2 (white) in PAs from TXNDC5$^{f/f}$ and TXNDC5^{ECKO} mice under normoxia and SuHx conditions. Nuclei were counterstained with DAPI (blue). L indicates lumen. Scale bars=20 μm. **G**, Western blots showing the protein levels of COL1A1, TGM2, FN1, POSTN, and LOX in hPAECs transferred with siTXNDC5 or siNC in normoxia or hypoxia conditions (n=6). Data represent the mean±SD. Comparisons of parameters were performed with the 2-way ANOVA, followed by the Tukey honestly significant difference test for multiple comparisons. ECM indicates extracellular matrix; PPI, protein-protein interaction; Nor, normoxia; Hyp, hypoxia; SuHx, Sugen5416/hypoxia; si, small interfering; α-SMA, α-smooth muscle actin; POSTN, periostin; BGN, biglycan; LOX, lysyl oxidase; TGM2, transglutaminase 2; FN1, fibronectin; and COL1A1, collagen alpha-1 chain.

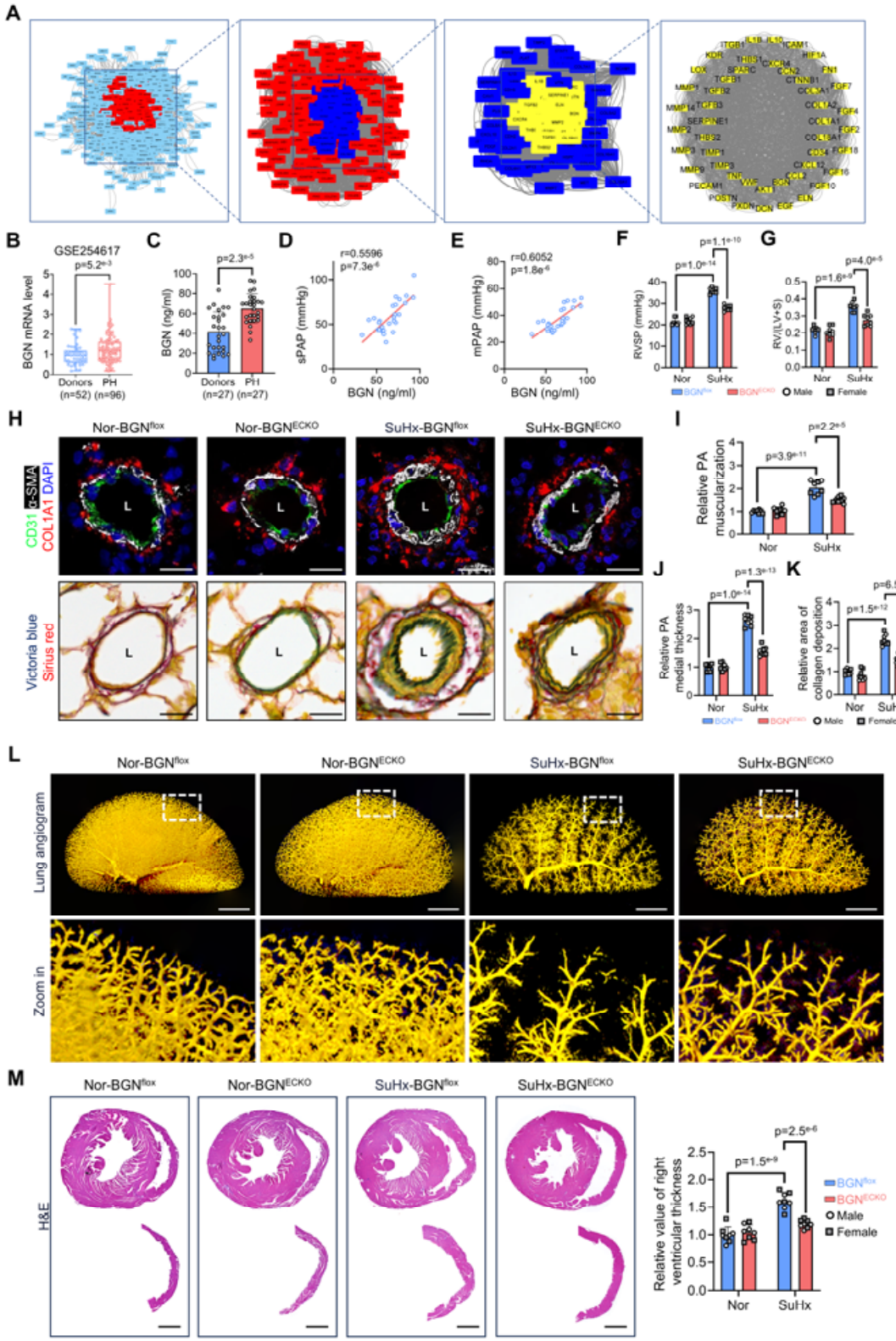

753

754 **Figure 5. BGN served as a biomarker and therapeutic target of PH.**

755 **A**, The progressive screening of the PPI network between ECM genes and ECs

756 function-related genes. Each new PPI network is composed of core genes in the

757 previous network. **B**, Box-whisker plot showing the relative mRNA levels of TXNDC5

in lung tissues from PH patients (n=96) and healthy donors (n=52) (GSE254617). **C**, Enzyme-linked immunosorbent assay showing the BGN level in the serum of non-PH donors (n=27) and patients with PH (n=27). **D-E**, Linear regression analysis showing the correlation between serum BGN concentrations with sPAP and mPAP of PH patients. **F**, Quantification of right ventricular systolic pressure (RVSP) in BGN^{flox} and BGN^{ECKO} mice exposed to normoxia or SuHx (n=8). **G**, Fulton index [RV/(LV+S)] in BGN^{flox} and BGN^{ECKO} mice exposed to normoxia or SuHx (n=8). **H**, Representative multiplex immunofluorescence (mIF) of distal pulmonary arteries (PAs) from BGN^{flox} and BGN^{ECKO} mice under normoxia or SuHx, showing CD31 (green), α-SMA (white), and COL1A1 (red), together with Victoria blue/Sirius red (VB/SR) staining of elastic lamina (dark blue), perivascular collagens (red), and muscle fiber (yellow). Nuclei were counterstained with DAPI (blue). L indicates lumen. Scale bars=25 μm. **I**, Quantification of distal PA muscularization based on α-SMA positive area (n=8). **J**, Medial wall thickness of distal PAs, measured across the elastic lamina visualized by VB staining (n=8). **K**, Quantification of collagen deposition of distal PAs from BGN^{flox} and BGN^{ECKO} mice under normoxia or SuHx(n=8). **L**, Representative lung angiogram of the left lungs from BGN^{flox} and BGN^{ECKO} mice treated with SuHx or under normoxic conditions. Scale bars=2 mm. **M**, Histological analysis of heart cross-sections at the mid-RV plane (top) and highlighted right ventricular wall (bottom) of the BGN^{flox} and BGN^{ECKO} mice exposed to normoxia or SuHx (n=8). Scale bars=1 mm. Data represent the mean±SD. Comparisons of parameters were performed with the 2-tailed Mann-Whitney *U* test (**B** and **C**), Pearson correlation test (**D** and **E**), or 2-way ANOVA (**F-G**, **I-K,** and **M**), followed by Tukey honestly significant difference test for multiple comparisons. H&E indicates hematoxylin-eosin; α-SMA, α-smooth muscle actin; COL1A1, collagen type I alpha 1; DAPI, 4′,6-diamidino-2-phenylindole; Nor, normoxia; SuHx, Sugen5416/hypoxia; RV, right ventricle; sPAP, systolic pulmonary arterial pressure; and mPAP, mean pulmonary arterial pressure.

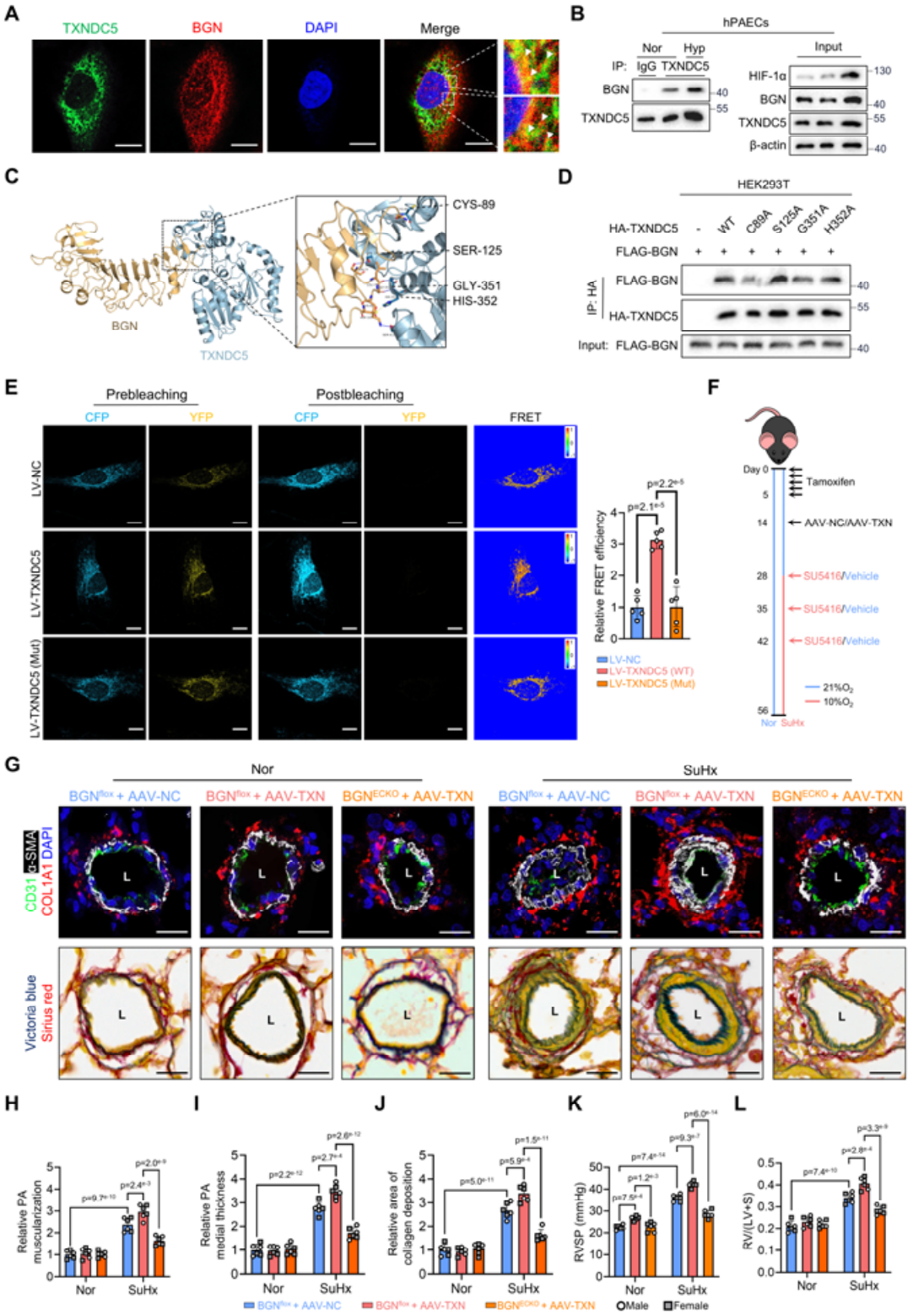

Figure 6. TXNDC5 assisted BGN protein folding to promote PH.

A, Immunofluorescence staining showing the localization of TXNDC5 (green) and BGN (red) in hPAECs. Nuclei (blue) were stained with DAPI. White arrows in the enlarged view indicate the colocalization of TXNDC5 with BGN (yellow). Scale

790 bars=10 μm. **B**, Coimmunoprecipitation analysis showing the interaction between
791 TXNDC5 and BGN in hPAECs under both normoxic and hypoxic situations. IP:
792 TXNDC5, immunoprecipitation with TXNDC5 antibody. IgG for the negative control.
793 **C**, Molecular docking showing the binding domains of human TXNDC5 and BGN. **D**,
794 Immunoprecipitation with anti-HA beads in HEK293T cells transfected with FLAG-
795 BGN and HA-TXNDC5 mutant plasmids. **E**, FRET acceptor photobleaching of the
796 hPAECs transfected with CFP-BGN-YFP plasmid. CFP and YFP images were taken
797 both before and after acceptor photobleaching. FRET efficiency is displayed as a
798 pseudocolor representation and qualification by ImageJ (n=5). Scale=10 μm. **F**,
799 Schematic of the *in vivo* rescue experiments: adeno-associated virus encoding
800 TXNDC5 (AAV-TXN) or control AAV (AAV-NC) was delivered to lung ECs in
801 BGN^{flox} and BGN^{ECKO} mice under normoxia or SuHx conditions. **G**, Representative
802 multiplex immunofluorescence (mIF) images of distal pulmonary arteries (PAs) from
803 BGN^{flox} and BGN^{ECKO} mice treated with AAV-NC or AAV-TXN, showing CD31
804 (green), α-SMA (white), and COL1A1 (red), with Victoria blue/Sirius red (VB/SR)
805 staining of elastic lamina (dark blue), perivascular collagens (red), and muscle fiber
806 (yellow). Nuclei stained with DAPI (blue). L indicates lumen. Scale bars=25 μm. **H**,
807 Quantification of distal PA muscularization in BGN^{flox} and BGN^{ECKO} mice with AAV-
808 NC or AAV-TXN administration (n=6). **I**, Medial wall thickness of distal PAs measured
809 across the elastic lamina, visualized by VB staining (n=6). **J**, Quantification of collagen
810 deposition area in distal PAs (n=6). **K**, Right ventricular systolic pressure (RVSP) in
811 BGN^{flox} and BGN^{ECKO} mice treated with AAV-NC or AAV-TXN under SuHx or
812 normoxia conditions (n=6). **L**, Fulton index [RV/(LV+S)] in BGN^{flox} and BGN^{ECKO}
813 mice with AAV-NC or AAV-TXN treatment (n=6). Data represent the mean±SD.
814 Comparisons of parameters were performed with the 1-way (**E**) or 2-way (**H-L**)
815 ANOVA, followed by the Tukey honestly significant difference test for multiple
816 comparisons. ECs, endothelial cells; Nor, normoxia; Hyp, hypoxia; IgG,
817 immunoglobulin G; α-SMA, α-smooth muscle actin; COL1A1, collagen type I alpha 1;
818 FRET, fluorescence resonance energy transfer; CFP, cyan fluorescent protein; and YFP,
819 yellow fluorescent protein.

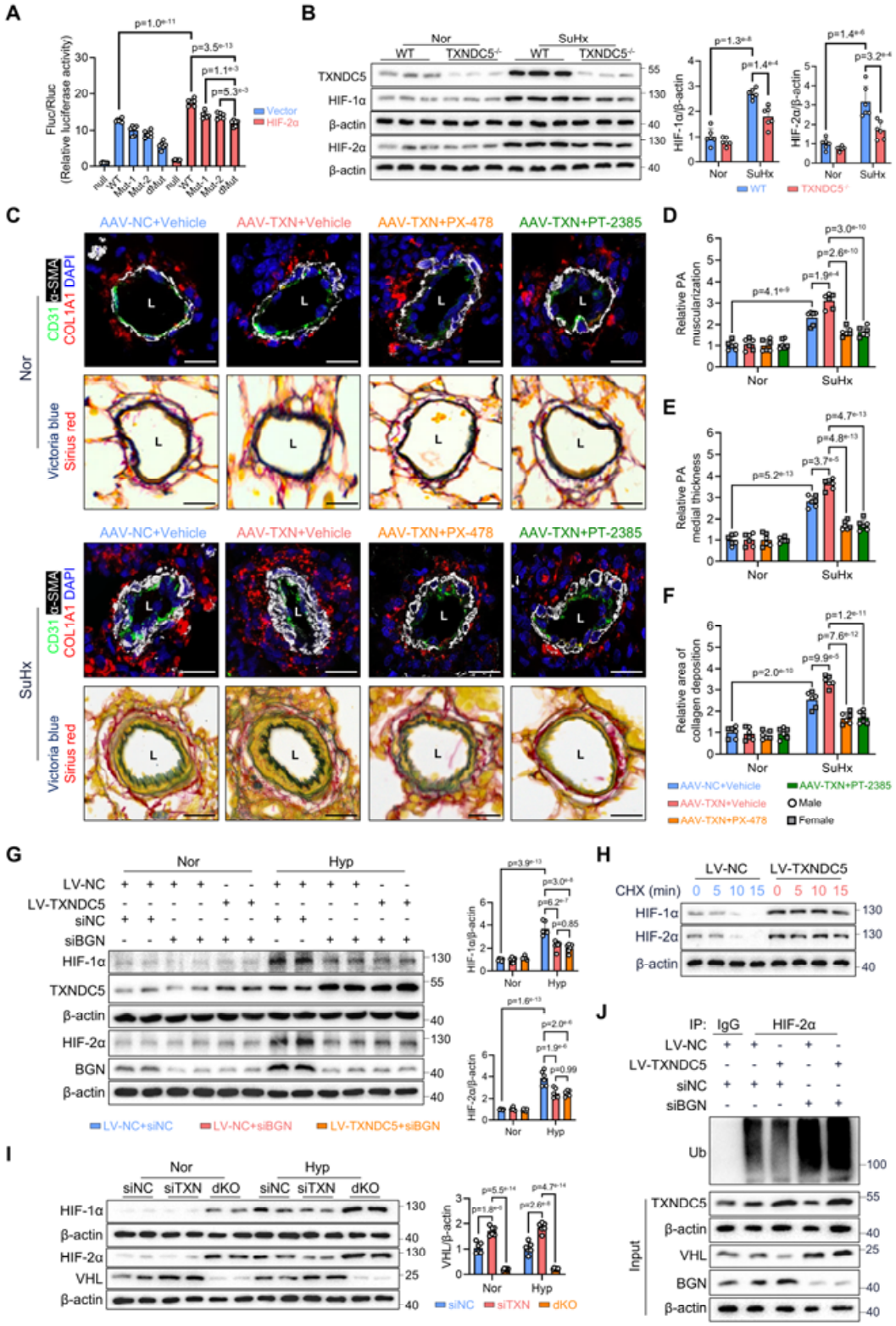

Figure 7. Endothelial TXNDC5 Driven PH via BGN-dependent stabilization of HIF-1α/2α.

A, Dual-luciferase assay showing that luciferase activity in constructs with BS1 mutation (Mut-1), BS2 mutation (Mut-2), or double mutation of BS1 and BS2 (dMut)

825 (n=6). **B**, Western blots showing the decreased protein levels of HIF-1α and HIF-2α in
826 the lungs from TXNDC5 deficiency mice compared with WT exposed to SuHx (n=6).
827 **C**, Representative distal pulmonary arteries (PAs) images from AAV-NC or AAV-TXN-
828 treated mice exposed to SuHx or normoxia, with HIF-1α inhibitor (PX-478) or HIF-2α
829 inhibitor (PT-2385), or vehicle administration. Multiplex immunohistochemical (mIF)
830 showing CD31 (green), α-SMA (white), and COL1A1 (red) and Victoria blue/Sirius red
831 (VB/SR) staining of elastic lamina (dark blue), perivascular collagens (red), and muscle
832 fiber (yellow). Nuclei were counterstained with DAPI (blue). L indicates lumen. Scale
833 bars=25 μm. **D**, **E**, and **F**, Quantitative analysis of distal PA remodeling, including PA
834 muscularization assessed by α-SMA-positive area (n=6), medial wall thickness
835 measured across the elastic lamina visualized by VB staining (n=6), and perivascular
836 collagen area quantified using SR staining (n=6). **G**, Representative Western blots
837 showing that the LV-TXNDC5-induced upregulation of HIF-1/2α was abolished by
838 siBGN in hPAECs both under normoxia and hypoxia conditions (n=6). **H**, Western blot
839 showing that the protein stabilization of HIF-1/2α was enhanced by LV-TXNDC5
840 treatment in hPAECs under normoxic conditions (n=5). **I**, Representative Western blots
841 of HIF-1α, HIF-2α, and VHL in hPAECs after treatment with TXNDC5 knockdown
842 only or double knockdown (dKO) of TXNDC5 and VHL (n=6). **J**, Western blot
843 analysis indicating the HIF-2α ubiquitylation profile was reduced by LV-TXNDC5 but
844 increased by siBGN treatment. hPAECs were treated with 10 μM MG132 for 6 h before
845 harvest. Data represent the mean±SD. Comparisons of parameters were performed with
846 2-way ANOVA, followed by the Tukey honestly significant difference test for multiple
847 comparisons. BS indicates binding site; VHL, von Hippel-Lindau; Ub, ubiquitin; Nor,
848 normoxia; Hyp, hypoxia; SuHx, Sugen5416/hypixa; IgG, immunoglobulin G; LV,
849 lentivirus; α-SMA, α-smooth muscle actin; and COL1A1, collagen type I alpha 1.

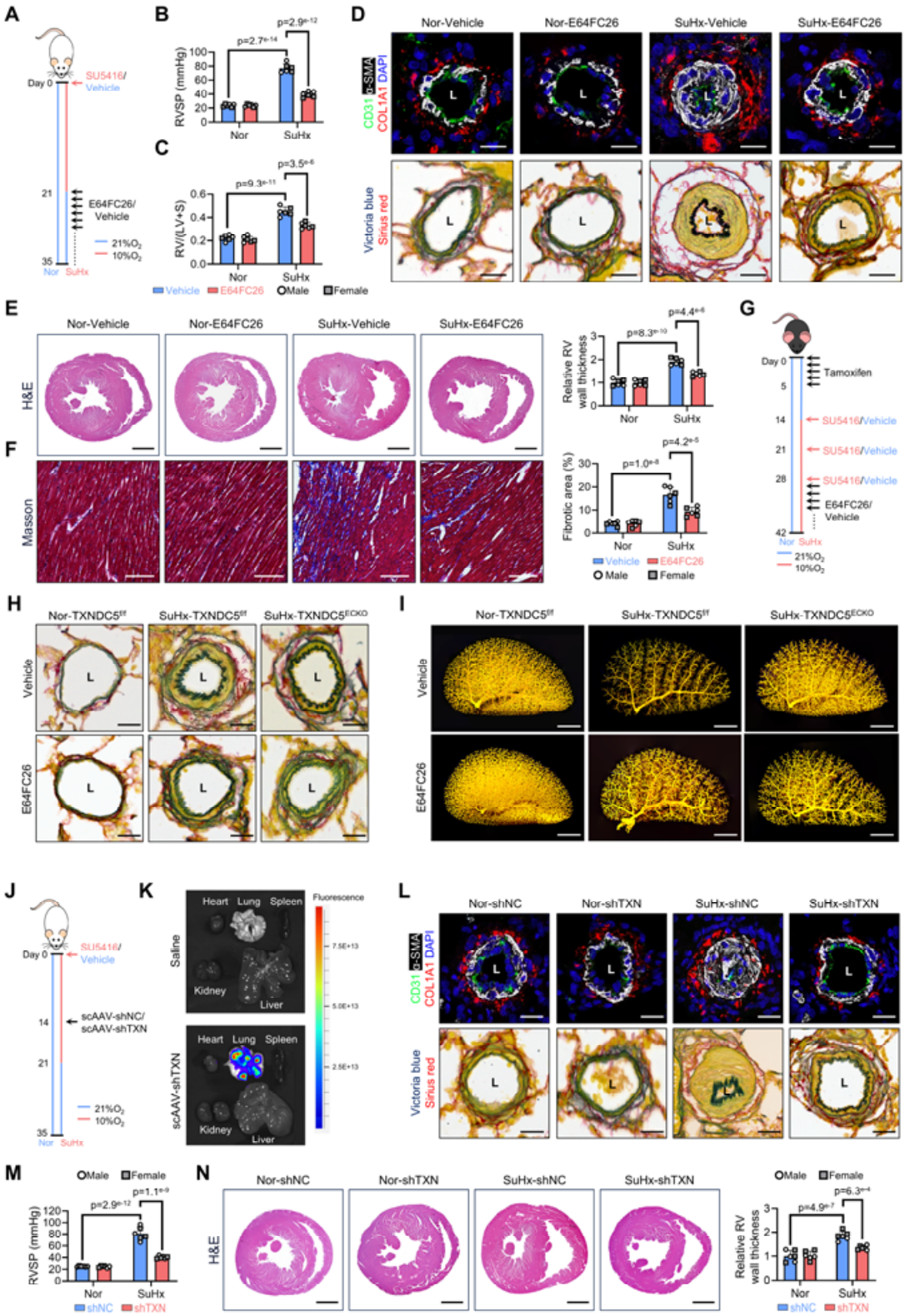

850

851 **Figure 8. Pharmacological and Pulmonary Endothelium-Targeted Inhibition of**

852 **TXNDC5 Ameliorated PH.**

853 **A**, Schematic protocol for E64FC26 administration for SuHx-induced PH rats. Rats

854 were treated with SuHx for 3 weeks and then intraperitoneal injection with 2 mg/kg

855 E64FC26 daily for 2 weeks under normoxic conditions. **B**, Quantification of right
856 ventricular systolic pressure (RVSP) in rats administered with E64FC26 or vehicle
857 exposed to normoxia or SuHx (n=6). **C**, Fulton index [RV/(LV+S)] of rats with
858 E64FC26 or vehicle treatment under normoxia or SuHx conditions (n=6). **D**,
859 Representative multiplex immunofluorescence (mIF) of distal pulmonary arteries (PAs)
860 from rats treated with vehicle or E64FC26 under normoxia or SuHx conditions,
861 showing CD31 (green), α-SMA (white), and COL1A1 (red), together with Victoria
862 blue/Sirius red (VB/SR) staining of elastic lamina (dark blue), perivascular collagens
863 (red), and muscle fiber (yellow). Nuclei were counterstained with DAPI (blue). L
864 indicates lumen. Scale bars = 25 μm. **E**, Histological and quantification analysis of the
865 cross-sectioned heart at the mid-RV plane (top) and the highlighted right ventricular
866 wall (bottom) of rats treated with E64FC26 or vehicle under normoxia or SuHx
867 conditions (n=6). Scale bars=2 mm. **F**, Masson's trichrome staining and quantification
868 of the fibrotic area by collagen volume fraction measured by Image J of RV from rats
869 treated with E64FC26 or vehicle exposed to normoxia or SuHx (n=6). Scale bars=100
870 μm. **G**, Schematic of vehicle or E64FC26 treatment in $TXNDC5^{f/f}$ and $TXNDC5^{ECKO}$
871 mice under SuHx conditions to investigate whether the effects of E64FC26 are
872 TXNDC5-dependent. **H**, Representative distal PAs images from $TXNDC5^{f/f}$ and
873 $TXNDC5^{ECKO}$ mice treated with vehicle or E64FC26 under SuHx or normoxia
874 conditions. Victoria blue/Sirius red (VB/SR) staining of elastic lamina (dark blue),
875 perivascular collagens (red), and muscle fiber (yellow). L indicates lumen. Scale
876 bars=25 μm. **I**, Representative lung angiogram of SuHx-treated $TXNDC5^{f/f}$ and
877 $TXNDC5^{ECKO}$ mice with or without E64FC26 administration, showing distal
878 pulmonary perfusion. Scale bars=2 mm. **J**, Schematic diagram of the pulmonary
879 endothelium-targeted gene therapy strategy. Rats received a tail vein injection of self-
880 complementary adeno-associated virus (scAAV) encoding shRNA against TXNDC5
881 (shTXN) or control shRNA (shNC). **K**, Representative IVIS images of major organs
882 from rats treated with Saline or scAAV-shTXN, showing GFP fluorescence delivered
883 by the scAAV vector. **L**, Representative mIF for CD31 (green), α-SMA (white), and
884 COL1A1 (red), and VB/SR staining for elastic lamina (dark blue), collagens (red), and

885 muscle fiber (yellow) in distal PAs from rats receiving shNC or shTXN exposed to
886 normoxia or SuHx. Nuclei were counterstained with DAPI (blue). L indicates lumen.
887 Scale bars=25 μm. **M**, Hemodynamic measurement of RVSP in SuHx-induced PH rats
888 treated with shNC or shTXN (n=6). **N**, Histological sections of the heart at the mid-RV
889 plane and quantification of right ventricular wall thickness from SuHx-induced PH rats
890 treated with shNC or shTXN (n=6). Scale bars = 2 mm. Data represent the mean±SD.
891 Comparisons of parameters were performed with 2-way ANOVA, followed by Tukey
892 honestly significant difference test for multiple comparisons. H&E indicates
893 hematoxylin-eosin; α-SMA, α-smooth muscle actin; COL1A1, collagen type I alpha 1;
894 shRNA, short hairpin RNA; f/f, flox/flox; Nor, normoxia; SuHx, Sugen5416/hypoxia;
895 and RV, right ventricle.

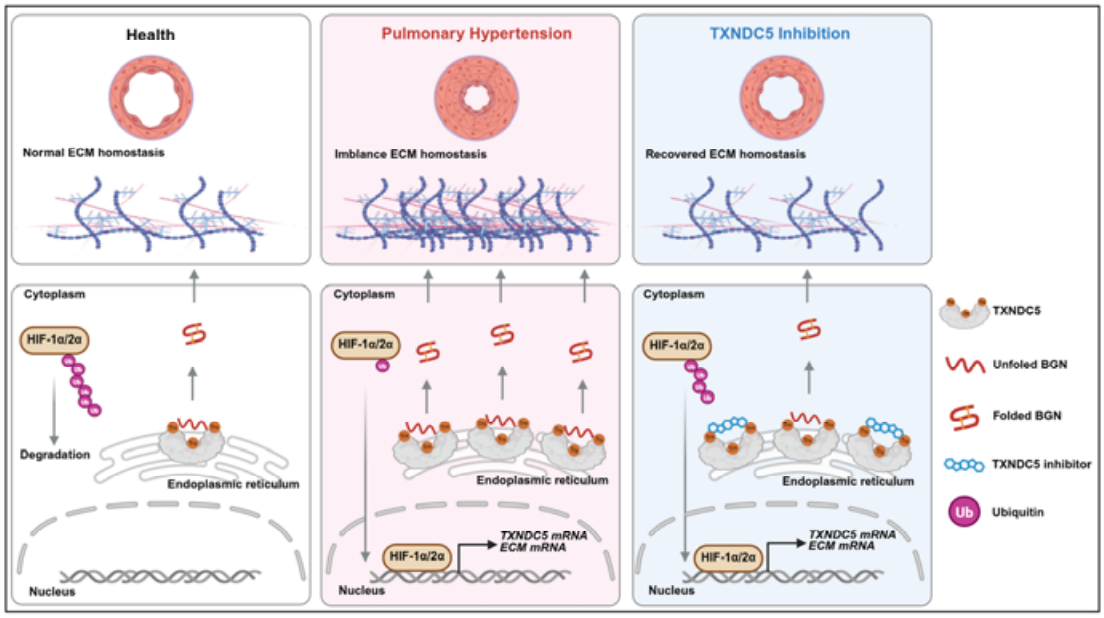

896

897 **Graphic Abstract.** The role of TXNDC5 in regulating ECM homeostasis during PH.
898 In the healthy state, BGN folding is properly maintained and HIF-1α/2α is rapidly
899 degraded. During PH, TXNDC5 is upregulated, leading to excessive accumulation of
900 BGN and impaired ubiquitination-mediated degradation of HIF-1α/2α, resulting in an
901 imbalance in ECM homeostasis and contributing to vascular remodeling.
902 Pharmacological or genetic inhibition of TXNDC5 restores BGN folding capacity and
903 facilitates HIF-1α/2α degradation, thereby reestablishing ECM homeostasis and
904 attenuating PH progression.

905 **Supplemental Figures**

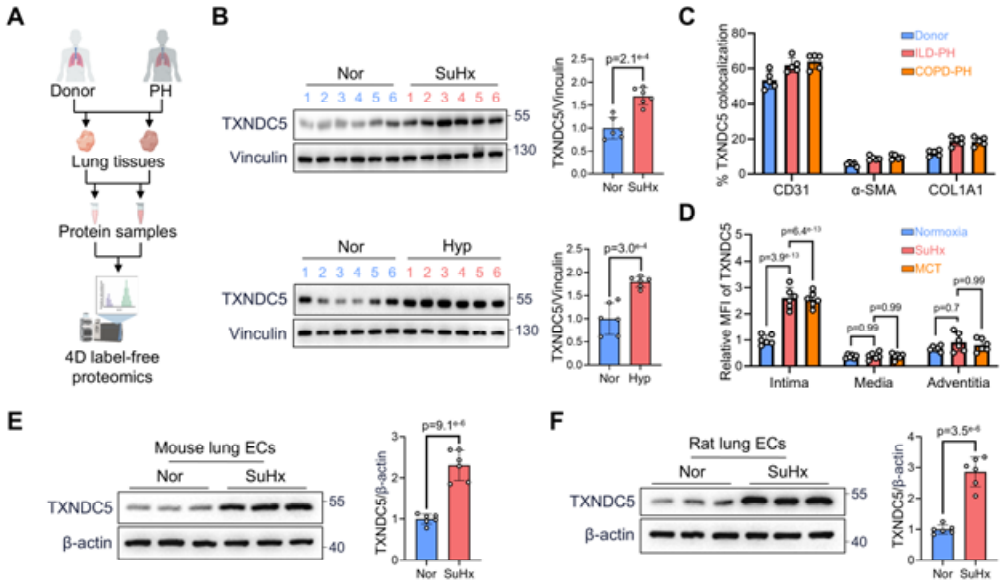

906

907 **Figure S1. Upregulation of TXNDC5 in the lungs and lung endothelial cells of PH**

908 **rodent models.**

909 **A**, Schematic illustration showing the 4D label-free proteomics of lungs from non-PH

910 donors and patients with hypoxic PH. **B**, Western blot analysis and quantification of
911 TXNDC5 and Vinculin in the lungs of mice exposed to SuHx or hypoxia or under
912 normoxic situations (n=6). **C**, Quantitative analysis of mIF showing TXNDC5 was
913 predominantly co-localized with CD31 in distal PAs. (n=5). **D**, Quantification of mean
914 fluorescence intensity (MFI) of TXNDC5 in remodeled distal PAs from SuHx- and
915 MCT-induced rat PH models compared with rats under normoxic conditions. (n=6). **E**,
916 Western blot of TXNDC5 in primary lung ECs from SuHx-induced mice or normoxic
917 controls, showing increased protein levels in ECs. **F**, Western blot of TXNDC5 in lung
918 ECs isolated from SuHx-induced PH rats, demonstrating elevated expression compared
919 with normoxic controls. Data represent the mean±SD. Comparisons of parameters were
920 performed with the unpaired 2-tailed Student *t*-test (**B**, **E**, and **F**) or 2-way ANOVA (**D**),
921 followed by Tukey honestly significant difference test for multiple comparisons. Nor
922 indicates normoxia; Hyp, hypoxia; SuHx, Sugen5416/hypoxia; and ECs, endothelial
923 cells.

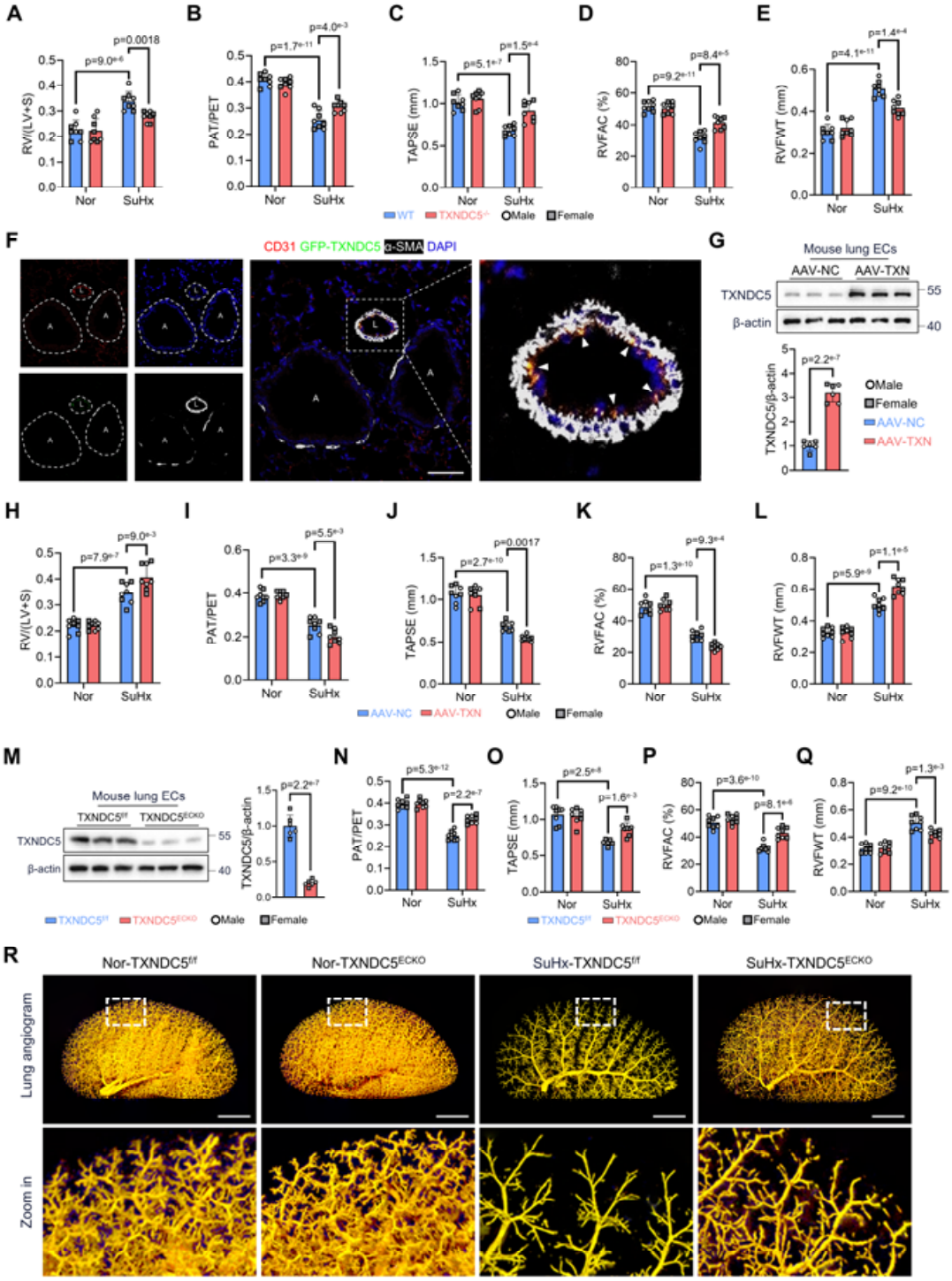

Figure S2. Role of TXNDC5 in PH development.

A, Fulton index [RV/(LV+S)] in WT and TXNDC5$^{-/-}$ mice exposed to normoxia or SuHx (n=8). **B**, **C**, **D**, and **E**, Echocardiography analysis of PAT/PET, TAPSE, RVFAC, and RVFWT in WT and TXNDC5$^{-/-}$ mice exposed to normoxia or SuHx (n=8). **F**,

929 Representative confocal images showing GFP-TXNDC5 (green), CD31 (red), and α-
930 SMA (white) in lung sections from AAV-TXN-treated mice. Nuclei were counterstained
931 with DAPI (blue). L indicates lumen. A indicates airway. Scale bars=50 μm. **G**, Western
932 blot analysis of TXNDC5 protein levels in primary lung ECs isolated from AAV-TXN-
933 or AAV-NC-treated mice (n=6). **H**, RV/(LV+S) in mice administered with AAV-NC or
934 AAV-TXN exposed to normoxia or SuHx (n=8). **I**, **J**, **K**, and **L**, Echocardiography
935 analysis of PAT/PET, TAPSE, RVFAC, and RVFWT in mice administered with AAV-
936 NC or AAV-TXN exposed to normoxia or SuHx (n=8). **M**, Representative Western blots
937 and quantification of TXNDC5 protein levels in primary lung ECs isolated from
938 $TXNDC5^{f/f}$ and $TXNDC5^{ECKO}$ mice (n=6). **N**, **O**, **P**, and **Q**, Echocardiographic
939 assessment of right ventricular function in $TXNDC5^{f/f}$ and $TXNDC5^{ECKO}$ under
940 normoxia or SuHx, including PAT/PET, TAPSE, RVFAC, and RVFWT (n=8). **R**,
941 Enlarged lung angiogram images of the left lungs from $TXNDC5^{f/f}$ and $TXNDC5^{ECKO}$
942 mice treated with SuHx or under normoxic conditions. Scale bars=2 mm. Data represent
943 the mean±SD. Comparisons of parameters were performed with the unpaired 2-tailed
944 Student *t*-test (**G** and **M**) or 2-way ANOVA (**A-E**, **H-L,** and **N-Q**), followed by Tukey
945 honestly significant difference test for multiple comparisons. Nor indicates normoxia;
946 SuHx, Sugen5416/hypoxia; PAT/PET, pulmonary artery acceleration time/pulmonary
947 artery ejection time ratio; TAPSE, tricuspid annular plane systolic excursion; RVFAC,
948 right ventricular fractional area change; RVFWT, right ventricular free wall thickness;
949 DAPI indicates 4′,6-diamidino-2-phenylindole; α-SMA, α-smooth muscle actin; and f/f,
950 flox/flox.

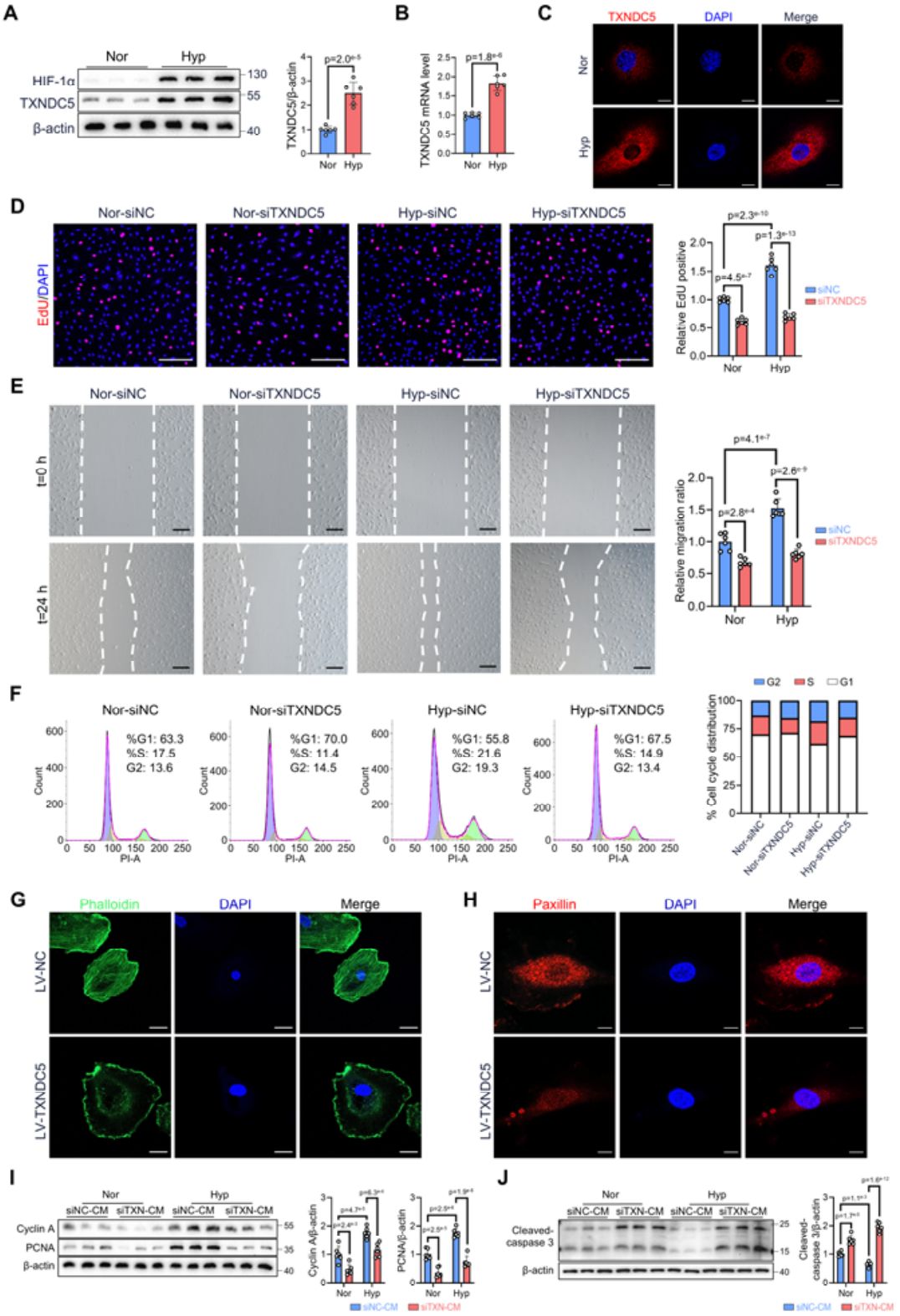

951

952 **Figure S3. TXNDC5 regulated cell function in pulmonary artery.**

953 **A** and **B**, Quantification of TXNDC5 protein levels by Western blots and TXNDC5

954 mRNA levels by qPCR analysis in hPAECs in both normoxia and hypoxia situations

955 (n=6). **C**, Immunofluorescence staining analysis showing increased protein levels of

956 TXNDC5 exposed to hypoxia. Scale bars=10 μm. **D**, Representative EdU (red) staining
957 image and group data showing the effects of TXNDC5 silencing on the proliferative
958 activity of hPAECs (n=6). Nuclei were counterstained with DAPI (blue). Scale
959 bars=200 μm. **E**, Representative images and group data showing the migration of
960 hPAECs treated with hPAECs siTXNDC5 or siNC in normoxia or hypoxia conditions
961 (n=6). Scale bars=200 μm. **F**, Flow cytometry showing the effect of siTXNDC5 on the
962 cell cycle of hPAECs exposed to normoxia or hypoxia. The representative images and
963 quantification of percentages of cells in G1, S, and G2 were shown (n=6). X and Y axes,
964 respectively, indicate the denoted DNA content stained with propidium iodide (PI) and
965 cell counts. **G** and **H**, Confocal microscopy images showing the effect of LV-TXNDC5
966 on the cytoskeletal architecture of hPAECs. Cells were stained with phalloidin (green,
967 scale bars=20 μm) or paxillin (red, scale bars=10 μm). Nuclei were counterstained with
968 DAPI (blue). **I** and **J**, Representative Western blots and quantification showing the
969 protein levels of Cyclin A, proliferating cell nuclear antigen (PCNA), and cleaved-
970 caspase 3 of hPASMCs treated with conditioned medium from hPAECs transfected with
971 siTXNDC5 or siNC in normoxia or hypoxia conditions (n=6). Data represent the
972 mean±SD. Comparisons of parameters were performed with the unpaired 2-tailed
973 Student *t*-test (**A** and **B**) or 2-way ANOVA (**D**, **E**, **I**, and **J**), followed by Tukey honestly
974 significant difference test for multiple comparisons. Nor indicates normoxia; Hyp,
975 hypoxia; LV, lentivirus; si, small interfering; CM, conditioned medium; and EdU, 5-
976 ethynyl-20-deoxyuridine.

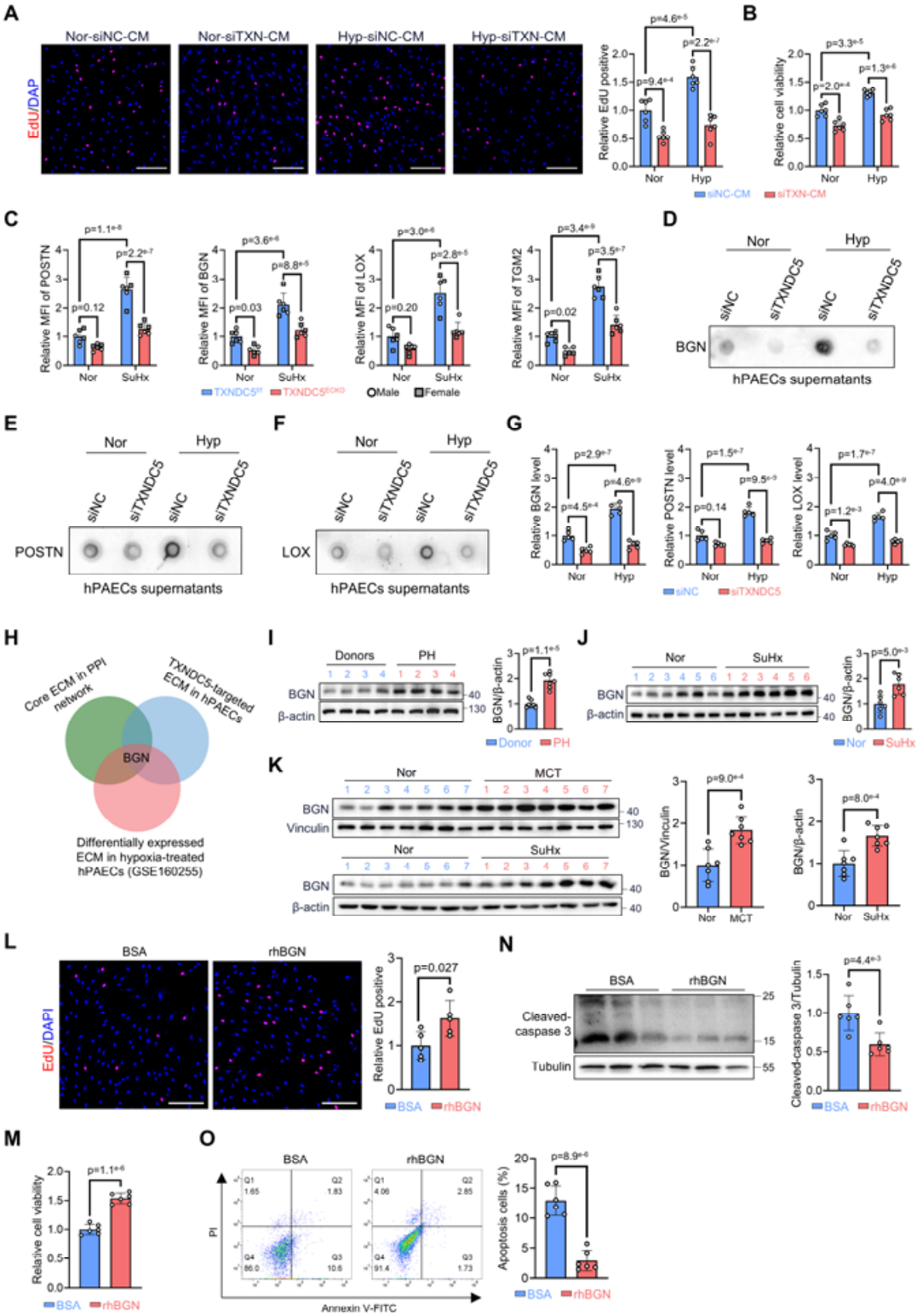

Figure S4. TXNDC5-driven endothelial paracrine signaling and ECM remodeling. **A**, Representative EdU staining image and group data showing the proliferative activity of hPASMCs treated with conditioned medium from hPAECs transfected with siTXNDC5 (siTXN-CM) or siNC (siNC-CM) in normoxia or hypoxia conditions (n=6).

982 Nuclei were counterstained with DAPI (blue). Scale bars=200 μm. **B**, CCK-8 assays
983 demonstrating decreased cell viability of hPASMCs after treatment with siTXN-CM or
984 siNC-CM (n=6). **C**, Quantification of POSTN, BGN, LOX, and TGM2 deposition in
985 distal PAs from SuHx-treated TXNDC5$^{f/f}$ and TXNDC5^{ECKO} mice, assessed by mean
986 fluorescence intensity (MFI) (n=6). **D**, **E**, and **F**, Representative dot blot analysis of
987 BGN, POSTN, and LOX in the supernatants of hPAECs transfected with siTXNDC5
988 or control siRNA (siNC). **G**, Quantification of dot blot intensities for BGN, POSTN,
989 and LOX, showing significantly reduced secretion upon TXNDC5 knockdown in
990 normoxia or hypoxia conditions (n=5). **H**, Venn diagram showing that BGN exists in
991 the overlapping of the core ECM genes in the PPI network, the differentially expressed
992 ECM proteins in TXNDC5 silencing hPAECs, and the differentially expressed ECM
993 genes in hypoxia-treated hPAECs (GSE160255). **I**, Representative Western blots and
994 quantification of BGN and vinculin in the lungs of donors and PH patients (n=7). **J**,
995 Representative Western blots and quantification of BGN and β-actin in the lungs from
996 mice exposed to SuHx or under normoxic conditions (n=6). **K**, Western blots showing
997 the BGN protein levels in the lungs collected from MCT or SuHx-treated rats or rats
998 under normoxia (n=7). **L**, Representative EdU staining image and group data showing
999 10 μg/ml recombinant human biglycan (rhBGN) treatment for 24 h enhanced the
1000 proliferative activity of hPASMCs (n=5). Scale bars=200 μm. **M**, CCK-8 assay
1001 confirming increased cell viability of hPASMCs after rhBGN treatment (n=6). **N**,
1002 Western blots showing the protein levels of cleaved-caspase 3 of hPASMCs treated with
1003 10 μg/ml rhBGN or the negative control (bovine serum albumin, BSA) for 24 h (n=6).
1004 **O**, Flow cytometry analysis of Annexin V-FITC/PI staining demonstrating decreased
1005 apoptotic cell populations in hPASMCs treated with rhBGN (n=6). Data represent the
1006 mean±SD. Comparisons of parameters were performed with the unpaired 2-tailed
1007 Student *t*-test (**I-O**) or 2-way ANOVA (**A-C** and **G**), followed by Tukey honestly
1008 significant difference test for multiple comparisons. Nor indicates normoxia; Hyp,
1009 hypoxia; SuHx, Sugen5416/hypoxia; MCT, monocrotaline; si, small interfering; DAPI,
1010 4′,6-diamidino-2-phenylindole; f/f, flox/flox; POSTN, periostin; BGN, biglycan; and
1011 LOX, lysyl oxidase; TGM2, transglutaminase 2.

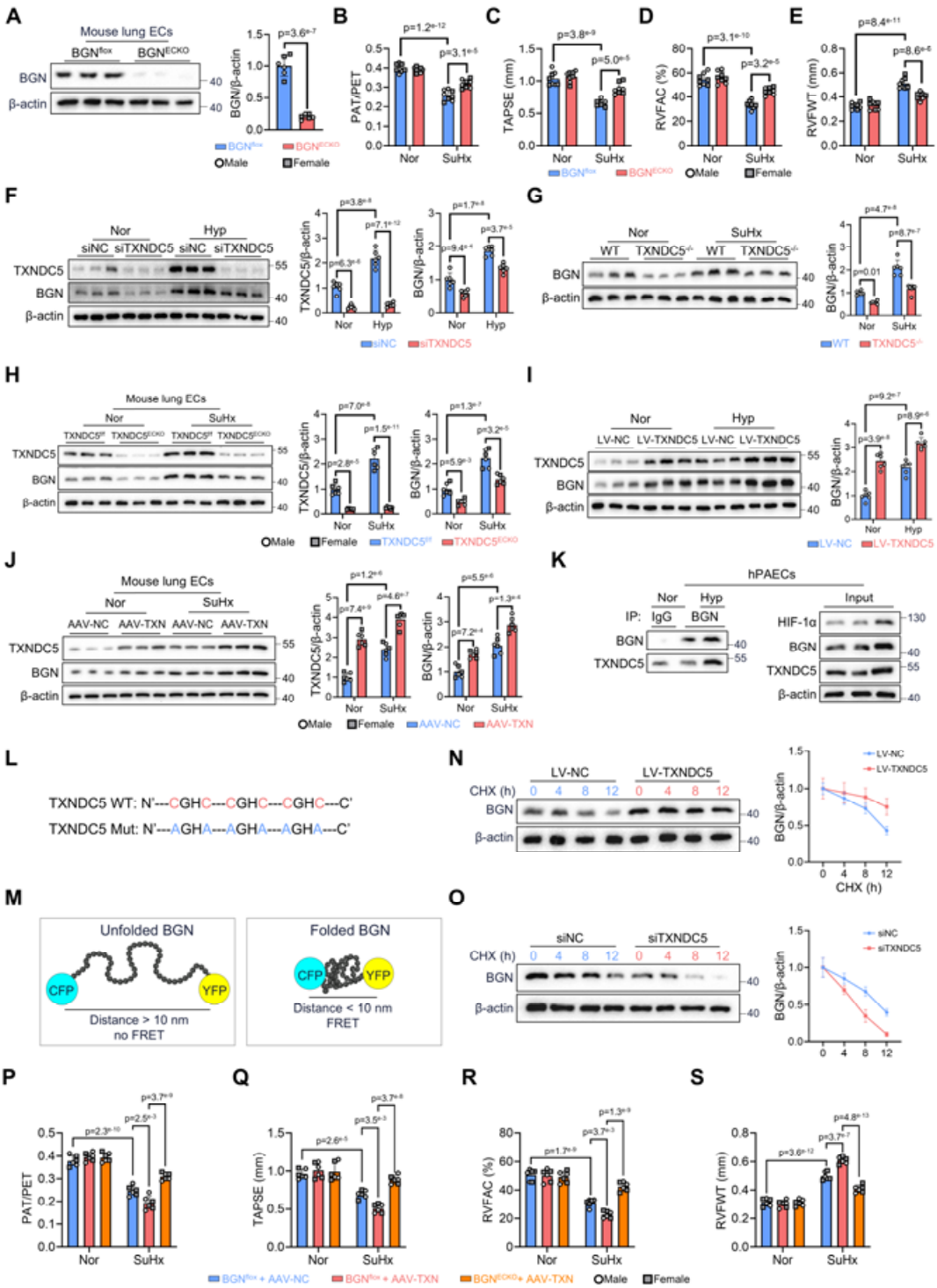

Figure S5. TXNDC5 stabilized BGN to regulate its protein expression.

A, Representative Western blots and quantification of BGN protein levels in primary lung ECs isolated from BGN^{flox} and BGN^{ECKO} mice (n=6). **B**, **C**, **D**, and **E**, Echocardiographic assessment of right ventricular function in BGN^{flox} and BGN^{ECKO}

1017 under normoxia or SuHx, including PAT/PET, TAPSE, RVFAC, and RVFWT (n=8). **F**,
1018 Representative Western blots and quantification of TXNDC5 and BGN in hPAECs
1019 treated with siNC or siTXNDC5 under normoxia or hypoxia conditions (n=6). **G**,
1020 Western blot analysis showing the downregulation of BGN in the lungs from TXNDC5
1021 deficiency mice compared with WT mice (n=6). **H**, Representative Western blots and
1022 quantification of TXNDC5 and BGN in lung ECs isolated from $TXNDC5^{f/f}$ and
1023 $TXNDC5^{ECKO}$ mice under normoxia or SuHx conditions (n=6). **I**, Representative
1024 Western blots showing that the LV-TXNDC5-induced upregulation of BGN in hPAECs
1025 both under normoxia and hypoxia conditions (n=6). **J**, Western blot analysis showing
1026 the upregulation of BGN in the lung ECs isolated from endothelial-specific AAV-NC
1027 or AAV-TXN-treated mice exposed to SuHx or under normoxic conditions (n=6). **K**,
1028 Coimmunoprecipitation analysis showing the interaction between TXNDC5 and BGN
1029 was enhanced by hypoxia stimulation in hPAECs. IP: BGN, immunoprecipitation with
1030 BGN antibody. IgG for the negative control. **L**, Scheme of WT (TXNDC5 WT) and
1031 mutant TXNDC5 (TXNDC5 Mut) sequences with Cysteine (C)-to-Alanine (A)
1032 mutations in all three thioredoxin domains. **M**, Schematic illustration for using FRET
1033 to determine the extent of BGN protein folding in hPAECs. When the BGN protein
1034 folds correctly (bottom), the distance between CFP and YFP will be less than 10 nm,
1035 resulting in FRET occurring. **N**, Western blot showing that TXNDC5 overexpression
1036 prolonged the BGN protein half-life in hPAECs (n=6). **O**, Western blot analysis
1037 demonstrating that TXNDC5 silencing destabilized BGN in hPAECs, resulting in
1038 accelerated protein degradation (n=6). **P**, **Q**, **R**, and **S**, Echocardiographic evaluation of
1039 right ventricular function in $BGN^{f/0(f/f)}$ and BGN^{ECKO} mice with AAV-NC or AAV-TXN
1040 treatment (n=6), including PAT/PET, TAPSE, RVFAC, and RVFWT (n=6). Data
1041 represent the mean±SD. Comparisons of parameters were performed with 2-way
1042 ANOVA, followed by the Tukey honestly significant difference test for multiple
1043 comparisons. Nor indicates normoxia; Hyp, hypoxia; SuHx, Sugen5416/hypoxia; IgG,
1044 immunoglobulin G; LV, lentivirus; WT, wild-type; Mut, mutation; CHX, cycloheximide;
1045 FRET, fluorescence resonance energy transfer; CFP, cyan fluorescent protein; YFP,
1046 yellow fluorescent protein; PAT/PET, pulmonary artery acceleration time/pulmonary

artery ejection time ratio; TAPSE, tricuspid annular plane systolic excursion; RVFAC, right ventricular fractional area change; and RVFWT, right ventricular free wall thickness.

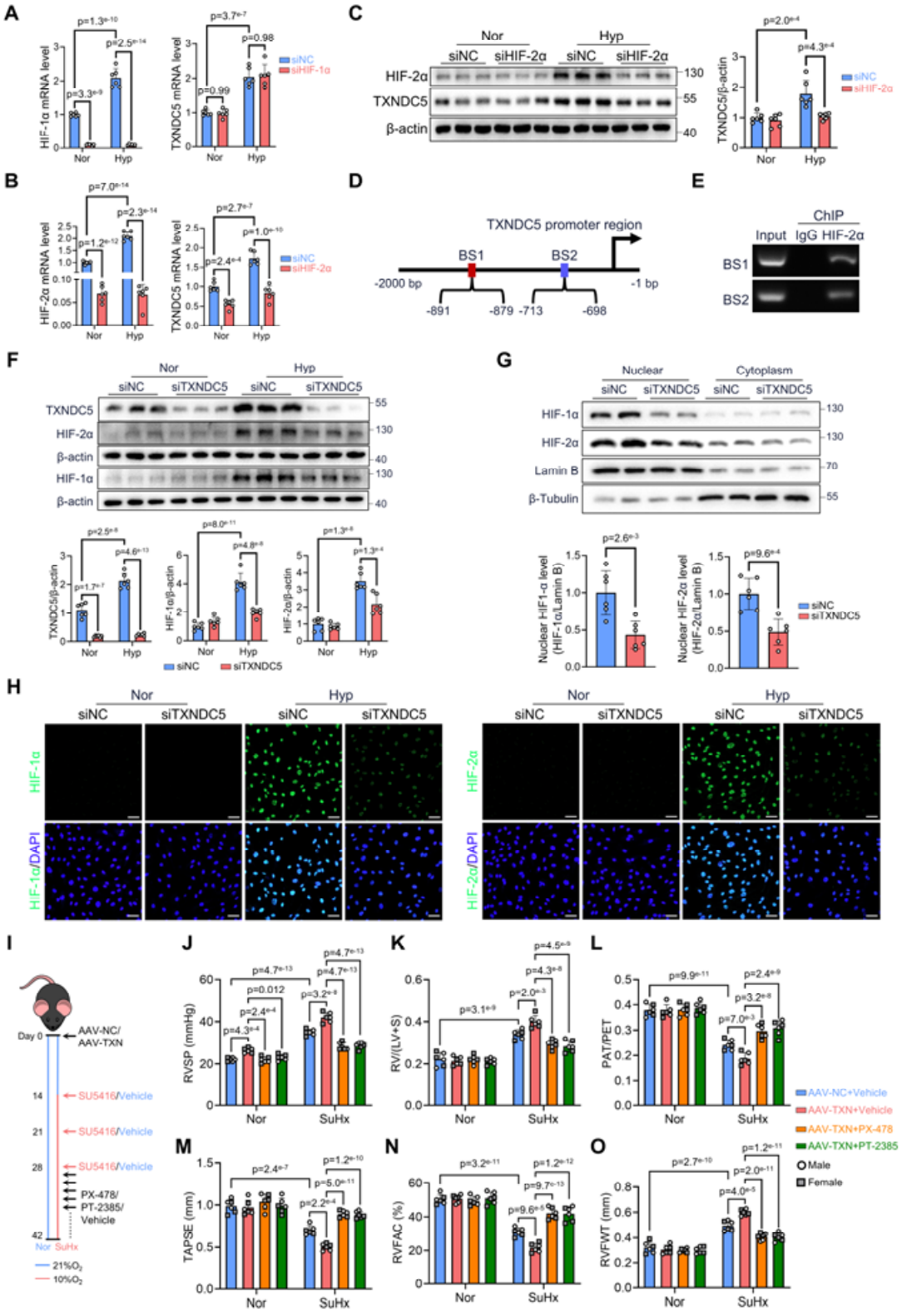

Figure S6. HIF signaling mediated TXNDC5-driven PH.

A and **B**, qPCR analysis showing the effects of HIF-1α (A) or HIF-2α (B) silencing on the mRNA expression of TXNDC5. Average expression values are normalized to the β-actin mRNA level. **C**, Western blot showing that siHIF-2α reduced the protein levels of TXNDC5 in hPAECs under hypoxic conditions (n=6). **D**, Schematic illustration showing 2 sites in HIF-2α predicted to bind to the TXNDC5 promoter region. **E**, Chromatin immunoprecipitation (ChIP) followed by polymerase chain reaction analysis showing that the BS1 and BS2 regions are both for HIF-2α binding. **F**, Western blot analysis showing that silencing of TXNDC5 reduced the protein levels of HIF-1α and HIF-2α in hPAECs under hypoxic conditions (n=6). **G**, Western blots showing that siTXNDC5 reduced the protein levels of HIF-1α and HIF-2α in the nucleus exposed to hypoxia in hPAECs (n=6). **H**, Immunofluorescent staining analysis showing that siTXNDC5 reversed the increased levels of HIF-1α (green, left) or HIF-2α (green, right) induced by hypoxia in hPAECs. Nuclei were counterstained with DAPI (blue). Scale bars=50 μm. **I**. Schematic diagram of the pharmacological rescue experiment. AAV-NC or AAV-TXN was delivered via the tail vein to overexpress TXNDC5 in lung endothelial cells of mice, followed by normoxia or SuHx exposure, and then with HIF-1α inhibitor (PX-478) or HIF-2α inhibitor (PT-2385), or vehicle treatment. **J**. Hemodynamic measurements showing right ventricular systolic pressure (RVSP) in mice treated as described in (I) (n=6). **K**, Fulton index [RV/(LV+S)] of mice, assessing right ventricular hypertrophy (n=6). **L**, **M**, **N,** and **O**, Echocardiographic evaluation of right ventricular function, including PAT/PET, TAPSE, RVFAC, and RVFWT (n=6). Comparisons of parameters were performed with the unpaired 2-tailed Student *t*-test (**G**) or 2-way ANOVA (**A-C**, **F,** and **J-O**), followed by Tukey honestly significant difference test for multiple comparisons. BS indicates binding site; Nor, normoxia; Hyp, hypoxia; SuHx, Sugen5416/hypixa; ChIP, chromatin immune precipitation; PAT/PET, pulmonary artery acceleration time/pulmonary artery ejection time ratio; TAPSE, tricuspid annular plane systolic excursion; RVFAC, right ventricular fractional area change; and RVFWT, right ventricular free wall thickness.

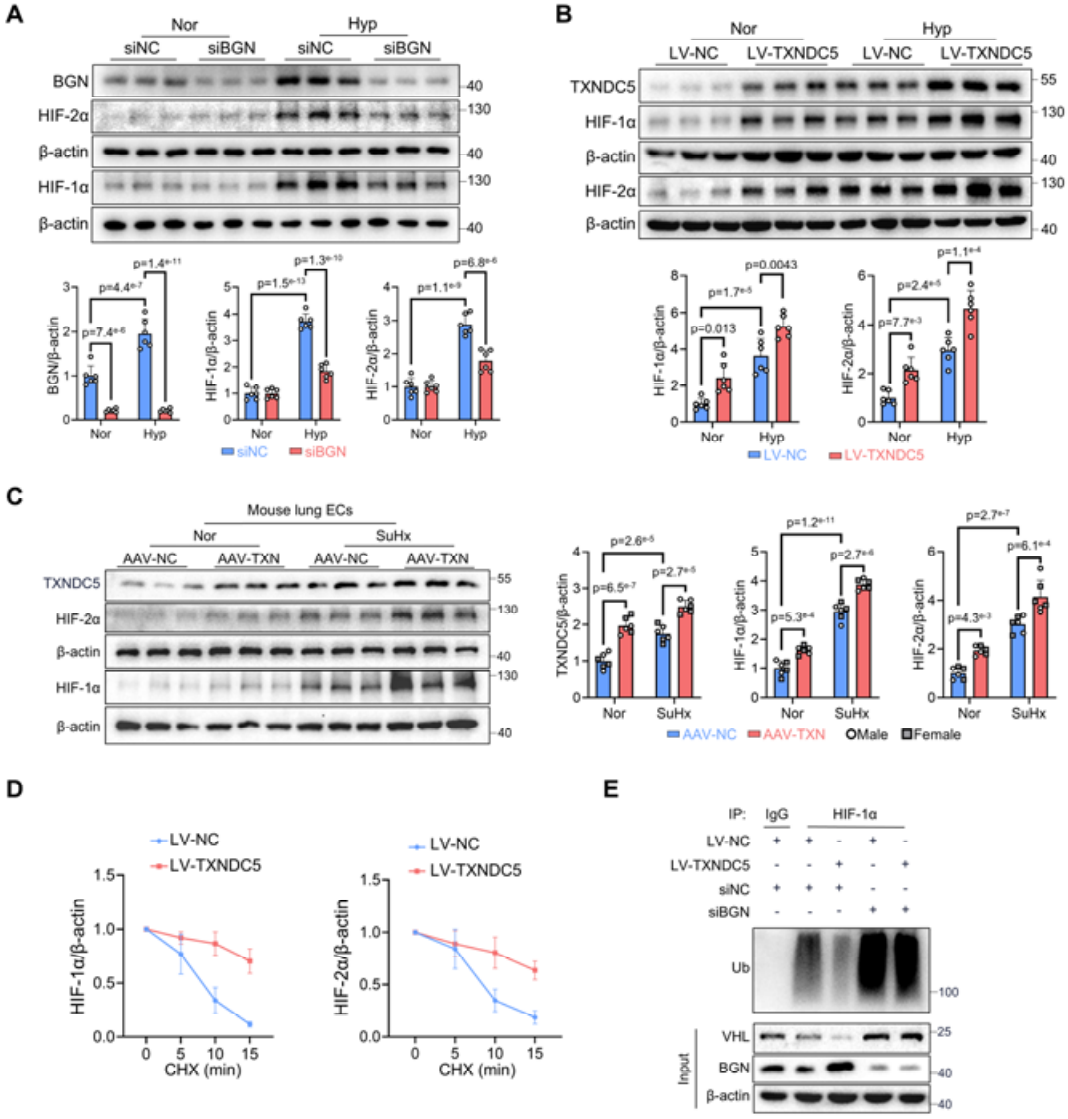

Figure S7. TXNDC5 inhibited the ubiquitination of HIF-1α/2α in a BGN-dependent manner.

A, Representative Western blots and quantification of BGN, and HIF-1/2α in hPAECs treated with siNC or siBGN under normoxia or hypoxia conditions (n=6). **B**, Western

1085 blot showing that the LV-TXNDC5-induced upregulation of HIF-1/2α in hPAECs both
1086 under normoxic and hypoxic situations (n=6). **C**, Representative Western blots and
1087 quantification of TXNDC5, HIF-1α, and HIF-2α in the lung ECs isolated from AAV-
1088 TXN or AAV-NC treated mice exposed to SuHx or under normoxic conditions (n=6).
1089 **D**, Quantification analysis showing that the protein half-life of endogenous HIF-1/2α
1090 was prolonged by LV-TXNDC5 treatment in hPAECs under normoxic conditions (n=5).
1091 **E**, Western blot analysis indicated that the HIF-1α ubiquitylation profile was reduced
1092 by LV-TXNDC5 but increased by siBGN treatment. hPAECs were treated with 10 μM
1093 MG132 for 6 h before harvest. Data represent the mean±SD. Comparisons of
1094 parameters were performed with the 2-way ANOVA, followed by the Tukey honestly
1095 significant difference test for multiple comparisons. Nor indicates normoxia; Hyp,
1096 hypoxia; SuHx, Sugen5416/hypoxia; Ub, ubiquitin; IgG, immunoglobulin G; AAV,
1097 adeno-associated viruses; LV, lentivirus; and CHX, cycloheximide.

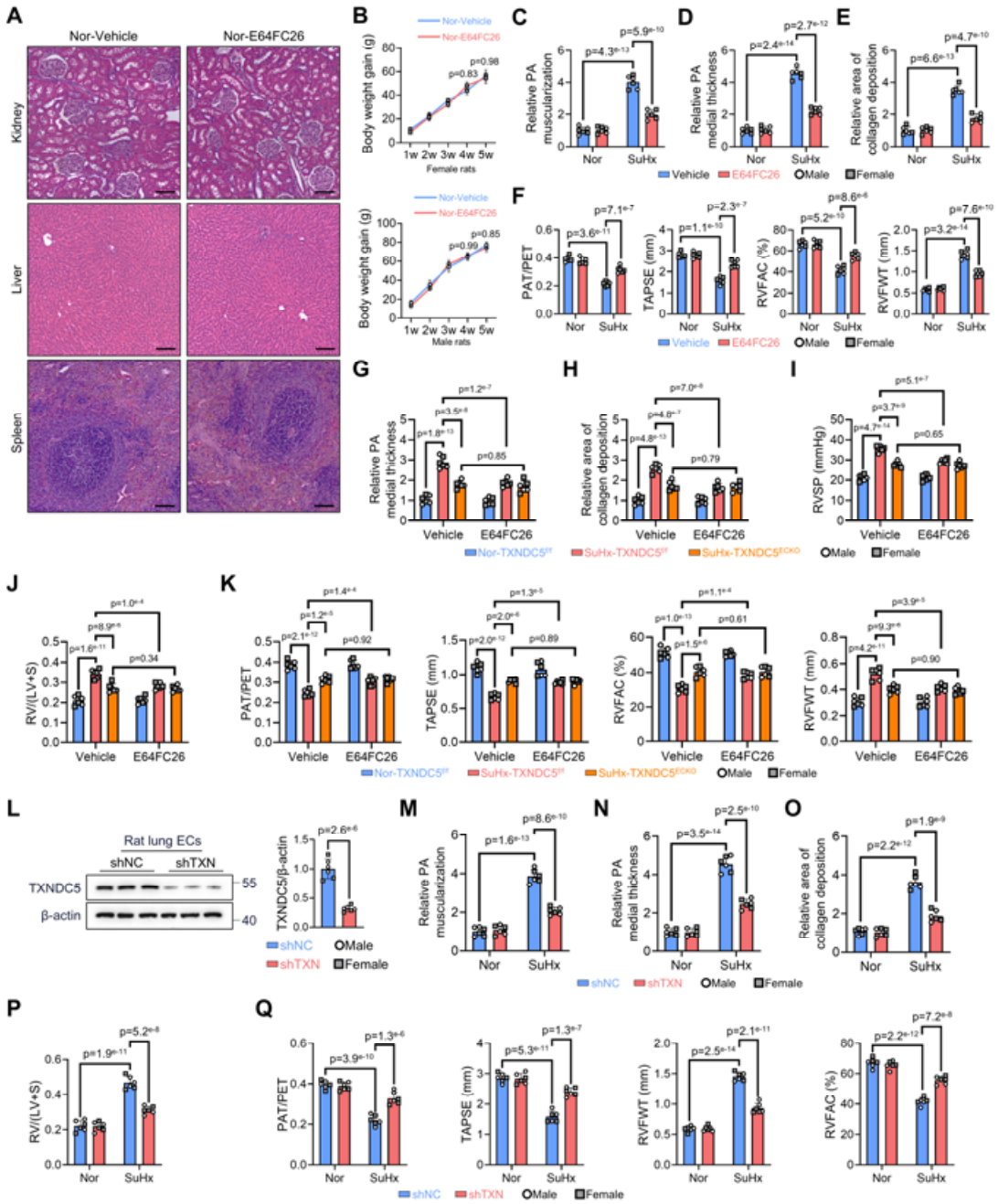

Figure S8. TXNDC5 inhibited the ubiquitination of HIF-1α/2α in a BGN-dependent manner.

A, Representative H&E staining of major kidney, liver, and spleen from rats maintained under normoxia for 5 weeks and continuously treated with E64FC26 or vehicle,

showing preserved tissue morphology without apparent injury or inflammation. Scale bars=100 μm. **B**, Gain of body weight of female (top panel) and male (bottom panel) rats maintained under normoxia for 5 weeks with E64FC26 or vehicle treatment (n=6). **C**, **D**, and **E**, Quantification of distal pulmonary arteries (PAs) remodeling in SuHx-induced PH rats treated with vehicle or E64FC26, including distal PA muscularization, medial wall thickness, and collagen deposition area (n=6). **F**, Echocardiographic assessment of right ventricular function in rats with vehicle or E64FC26 treatment, including PAT/PET, TAPSE, RVFAC, and RVFWT (n=6). **G** and **H**, Quantification of distal PA medial wall thickness and collagen deposition area SuHx-treated $TXNDC5^{f/f}$ and $TXNDC5^{ECKO}$ mice with or without E64FC26 administration under SuHx or normoxia conditions (n=6). **I**, Right ventricular systolic pressure (RVSP) in $TXNDC5^{f/f}$ and $TXNDC5^{ECKO}$ mice treated with vehicle or E64FC26 (n=6). **J**, Fulton index [RV/(LV+S)] of $TXNDC5^{f/f}$ and $TXNDC5^{ECKO}$ mice with vehicle or E64FC26 treatment (n=6). **K**, Echocardiographic assessment of right ventricular function in $TXNDC5^{f/f}$ and $TXNDC5^{ECKO}$ mice treated with vehicle or E64FC26 exposed to SuHx or normoxia, including PAT/PET, TAPSE, RVFAC, and RVFWT (n=6). **L**, Western blot showing efficient knockdown of TXNDC5 in lung ECs isolated from rats receiving pulmonary endothelium-targeted self-complementary adeno-associated virus (scAAV) carrying shRNA against TXNDC5 (shTXN) compared with control shRNA (shNC) (n=6). **M**, **N**, and **O**, Quantification of distal PA remodeling in SuHx-induced PH rats treated with shNC or shTXN, including distal PA muscularization, medial wall thickness, and perivascular collagen deposition area (n=6). **P**, Fulton index [RV/(LV+S)] in rats treated with shNC or shTXN under normoxia or SuHx conditions (n=6). **Q**, Echocardiographic assessment of right ventricular function in rats receiving shNC or shTXN, including PAT/PET, TAPSE, RVFAC, and RVFWT (n=6). Data represent the mean±SD. Comparisons of parameters were performed with the unpaired 2-tailed Student *t*-test (**L**) or 2-way ANOVA (**B**-**K**, and **M**-**Q**), followed by Tukey honestly significant difference test for multiple comparisons. H&E indicates hematoxylin-eosin; f/f, flox/flox; Nor, normoxia; SuHx, Sugen5416/hypoxia; shRNA, short hairpin RNA; PAT/PET, pulmonary artery acceleration time/pulmonary artery ejection time ratio;

TAPSE, tricuspid annular plane systolic excursion; RVFAC, right ventricular fractional area change; and RVFWT, right ventricular free wall thickness.